Meteorins regulate the formation of the left-right organizer and the establishment of vertebrate body asymmetry

Fanny Eggeler[1], Jonathan Boulanger-Weill[1#], Flavia De Santis[2,3#], Laura Belleri[1#], Karine Duroure[1], Thomas O. Auer[2,4], Shahad Albadri[1*], Filippo Del Bene[1,5*]

[1] Sorbonne Université, INSERM, CNRS, Institut de la Vision, F-75012 Paris, France
[2] Institut Curie, PSL Research University, Inserm U934, CNRS UMR3215, Paris, France
[3] ZeClinics SL. Sant Feliu de Llobregat, Barcelona, Spain.
[4] Department of Biology, University of Fribourg, Fribourg, Switzerland
[5] Lead contact

[#] These authors contributed equally
* correspondence: shahad.albadri@inserm.fr; filippo.del-bene@inserm.fr

SUMMARY

While the exterior of vertebrate bodies appears bilaterally symmetrical, internal organ positioning and morphology frequently exhibit left-right (L-R) asymmetries. In several vertebrates, including human, mouse, frog and zebrafish, left-right symmetry-breaking during embryonic development is initiated by a ciliated organ called the Node or left-right organizer. Within the Node, a leftward flow of extraembryonic fluid named the Nodal flow mediates the asymmetric expressions of Nodal factors. Although downstream Nodal pathway components leading to the establishment of the embryonic left-right axis are well known, less is known about the development and formation of the embryonic Node itself.

Here we reveal a novel role for the Meteorin protein family in the establishment of the left-right axis and in the formation of the Kupffer's vesicle, the Node equivalent structure in zebrafish. We show that the genetic inactivation of each or all three members of the zebrafish Meteorin family (*metrn*, *metrn-like a* and *metrn-like b*) leads to defects in properties of the Kupffer's vesicle, caused by impaired assembly and migration of the Kupffer's vesicle forming dorsal forerunner cells. In addition, we demonstrate that Meteorins genetically interact with integrins ItgaV and Itgβ1b regulating the dorsal forerunner cell clustering and that *meteorins* loss-of-function results in disturbed Nodal factor expression and consequently in randomized or symmetric heart looping and jogging.

These results identify a new role for the Meteorin protein family in the left-right asymmetry patterning during embryonic vertebrate development.

INTRODUCTION

From the outside the vertebrate body plan appears bilaterally symmetric. However, internal organs positioning and morphology often displays left-right (L-R) asymmetries. For instance, in vertebrates the heart generally lies on the left side, the liver and the pancreas are positioned on the right and the gut presents asymmetric rotations.

One major regulator for the establishment of the L-R axis is Nodal, a ligand belonging to the TGFβ protein family [1–6]. Its signaling is activated in the left lateral plate mesoderm (LPM), whereas Nodal remains inactive in the right LPM, creating an embryo-scale left-right asymmetry [3]. In mice, this asymmetry is achieved by an oriented rotation of the cilia of a structure called the Node generating a leftward flow of extraembryonic fluid named the Nodal flow. This results in an asymmetric expression of several Nodal factors and Nodal signaling. Participating in this patterning, Leftys, soluble inhibitors belonging to a subclass of TGF factors, antagonize Nodal signaling [7,8].

The Node and the Nodal flow have been described in numerous vertebrates. For instance, in *Xenopus* the gastrocoel roof plate and in zebrafish the Kupffer's vesicle (KV) [9–14] are key structures of the L-R symmetry breaking during the embryonic development [11,13,15]. Similarly, in humans and other mammals like rabbits and mice, the systematic establishment of left-right body symmetry begins with asymmetric fluid flow driven by rotating cilia [16]. This occurs within the transient primitive node in humans or the embryonic node in mice and rabbits [13,15,17]. However, in other mammalian classes, although left-right symmetry breaking mechanisms are believed to be cilia-independent, they are still poorly understood at present [2,18]. In chick, the symmetry breaking structure known as the Hensen's node, serves as the ciliated organizer responsible for the left-right asymmetry establishment. In this species, the process of symmetry breaking is believed to occur independently of the non-motile cilia present within the Hensen's node. Instead, the breaking of symmetry is primarily attributed to the leftward movement of cells around the node [19–21].

Compared to the relatively flat-shaped mouse node, the zebrafish KV is a fluid-filled sphere with a ciliated epithelium and it is formed by dorsal forerunner cells (DFCs) [9]. DFCs first emerge as cells of the epithelium of the dorsal surface in direct contact with the yolk syncytial layer at 6 hours post-fertilization (hpf) [22]. Around 8 to 9 hpf, following the epibolic movement, 20 to 30 DFCs form a single cluster and migrate towards the vegetal pole in a non-involuting manner at the leading edge [22,23]. During this migration process, polarized DFCs organize into multiple focal points by retaining long-lasting apical contacts within the cluster and remaining delaminated DFCs maintain contact with the cluster by cell-cell contact mechanisms [22,24]. At the final phase of epiboly and after reaching the vegetal pole, the DFC cluster is separating from the dorsal marginal enveloping layer cells by losing the apical contacts [22,24].

The focal points of the cluster are then rearranged by integrating the unpolarized DFCs to form a single focal point that will expand into a monolayer rosette structure containing a lumen to form the KV by 12 hpf [9,22–24]. Along this process, non-motile and motile monocilia are generated on the apical membrane facing the lumen that create a counterclockwise flow of fluid by the KV, called Nodal flow [22,25]. It was shown that the leftward directed flow within the KV results in asymmetric expression of zebrafish Nodal genes, like *spaw*, *lefty1* and *lefty2* that is fundamental for proper L-R patterning [26,27]. However, the molecular mechanisms involved in correct DFC migration and clustering that will form the KV remain largely elusive.

In this context, it has been reported that *nodal, lefty* as well as *p-smad2* expression are downregulated in *Meteorin*-null ES-cells. As such, Meteorin (Metrn) was hypothesized to be a novel important regulator of Nodal transcription [28].

Meteorin (Metrn), a secreted neurotrophic factor highly conserved among vertebrates, is expressed during early mouse development. It is already detected at the blastocyst stage in the inner cell mass and then expands through the extraembryonic ectoderm to the central (CNS) and peripheral nervous system (PNS) during later developmental stages [28]. It was first described to induce glial cell differentiation and to promote axonal extension in dorsal root ganglion (DRG) explants *in vitro* [29]. The disruption of *Metrn* function in Mouse resulted in early embryonic lethality [28] preventing the investigation of Metrn proteins function during early embryonic development *in vivo* and in particular their role for L-R patterning. Also conserved among vertebrates, its paralog Meteorin-like (Metrnl) has been first reported as a downstream target of the Pax2/5/8 signaling pathway during otic vesicle development [30] and was later shown to have neurotrophic properties comparable to the ones of Metrn [31].

Here, using the zebrafish larva as a model system, we generated knockout lines for all three-existing zebrafish *metrn* genes (*metrn*, *metrnla* and *metrnlb*). While all three single and compound mutants are viable, *metrns* mutant embryos displayed organ patterning defects notably with randomized or symmetric heart looping at a significantly higher frequency. Like in mice, *metrn* genes are expressed during early development already from the 2-cells stage and transcripts are detected in DFCs as well as in the KV structure. We show that *metrns* loss of function leads to DFC disorganization and Nodal flow formation defects within the KV. Together our study reveals a critical role for Metrn proteins in the DFC clustering, KV formation and in the establishment of the L-R axis.

112 **RESULTS**

113

114 **Metrns loss-of-function affects proper heart looping and correct visceral organs**
115 **positioning**

116 To study the functions of Meteorin proteins during early development, we generated knock out
117 zebrafish lines using the CRISPR/Cas9 technology to target the second exon of each gene
118 that encodes for the signal peptide sequence. The newly generated zebrafish mutant lines
119 carried out-of-frame deletions in the coding sequence of *metrn*, *metrnla* and *metrnlb* (Fig. S1A).
120 In contrast to published embryonic lethal *Metrn* mouse mutants [28], constitutive homozygote
121 zebrafish mutants for all three genes individually (*metrn*$^{-/-}$; *metrnla*$^{-/-}$; *metrnlb*$^{-/-}$), in double
122 (*metrn*$^{-/-}$, *metrnla*$^{-/-}$; *metrn*$^{-/-}$, *metrnlb*$^{-/-}$; *metrnla*$^{-/-}$, *metrnlb*$^{-/-}$) and triple (*metrn*$^{-/-}$, *metrnla*$^{-/-}$,
123 *metrnlb*$^{-/-}$ or triplMut), were all viable and did not show any obvious morphological defects (Fig.
124 1A).

125 We first validated that our mutagenic approach resulted in the generation of null alleles. To do
126 so, we performed *in situ* hybridization on *metrn*, *metrnla* and *metrnlb* from 2-cells stage to 1
127 day post-fertilization (dpf) on triplMut embryos (Fig. S1B). No expression could be detected for
128 neither of those two genes in the triplMut embryos, indicating the degradation of the transcripts
129 in the *metrn* mutant backgrounds (Fig. S1B). To confirm this observation, we compared the
130 expression level of all three *metrn* genes upon total mRNA extraction from 14 and 48 hpf WT
131 and triplMut embryos by qRT-PCR. *Metrn* and *metrnla* expression was detected in samples of
132 14 hpf WT embryos and *metrnlb* expression was detected in samples of 48 hpf WT embryos.
133 A significant reduction of the expression of all *metrn* genes could be measured using triplMut
134 samples of the same age. These results suggest that the mRNA produced by the loci that we
135 targeted is degraded by nonsense-mediated decay (Fig. S1C).

136 Despite the absence of gross morphological defects, using *myl7* antisense riboprobe *in situ*
137 hybridization in single mutant embryos, we observed a mis-positioning of the heart in triplMut
138 mutant embryos. Indeed while 88.43% of the wild type control embryos had D-looped shaped
139 hearts, only 38.17% of the triplMut embryos exhibited a WT-like heart looping phenotype
140 (Table 1 and Fig. 1B-C). Similarly, *metrn*$^{-/-}$ and *metrnla*$^{-/-}$ single mutant embryos displayed a
141 high proportion of randomized heart phenotypes, whereas *metrnlb*$^{-/-}$ single mutant embryos
142 showed a small percentage of heart looping phenotypes (Table 1 and Fig. 1B-C). The injection
143 of *metrn* and/or *metrnla* mRNA into one-cell stage triplMut zebrafish embryos could partially
144 rescue the observed phenotypes (Table 1, Fig. S1D). In addition to the heart, morphological
145 L–R asymmetry of the visceral organs was also perturbed in triplMut embryos (using *gata6*
146 expression as a marker). Indeed, 10.49% of the triplMut embryos exhibited symmetrical
147 placement of the gut and pancreas with respect to the midline and 9.88% *situs inversus* or
148 heterotaxy phenotypes compared to wild type embryos (WT: 93.84% L–R asymmetry, 4.79%

149 L–R symmetry and 1.37% heterotaxia) (Fig. 1D-E). These results indicate that while Metrns
150 are not implicated in the specification of neither the heart nor the visceral organs (*myl7* and
151 *gata6* expression being detected in triplMut embryos and in single mutants for *metrns*), their
152 loss of function reveal that they are implicated in the L-R asymmetry positioning of these
153 organs. The left-jogged and D-looped heart or the right-positioned liver are two of many
154 examples of early L-R asymmetry determination in zebrafish and are well-studied readouts for
155 altered L-R patterning processes. Therefore, our results suggest that Metrns, in particular
156 Metrn and Metrnla, may have a crucial function in establishing L-R asymmetry during the early
157 stages of development. To exclude potential genetic compensation effects among paralogs
158 that were reported in other studies [32], we focused all subsequent analyses (if not stated
159 otherwise) on the triple mutant line (triplMut).
160
161 **Metrns are required for proper Nodal factor gene expression**
162 Nodal signaling is one of the major regulatory pathways for the determination of the L-R axis
163 during vertebrate development. In zebrafish, null mutants for several Nodal factors like *spaw*
164 (*Nodal* zebrafish orthologue), *dand5* or *lefty1* (*lft1*) all display symmetric or randomized heart
165 looping and jogging similarly to *Nodal* mutant mice [33–36]. We therefore asked whether
166 Metrns loss of function could affect the expression of these factors. To do so, we assessed
167 *dand5*, *spaw*, *lft1* and *lft2* expression in our *metrns* mutant embryos. By qRT-PCR, we
168 measured a significant reduction of *dand5* expression at 14 hpf in triplMut embryos compared
169 to wild type controls (Fig. 2A). Similarly, the expression of *spaw*, *lft1* as well as *lft2* in the
170 absence of Metrns proteins was also downregulated in triplMut embryos compared to wild type
171 embryos (Fig. 2A).
172 In order to assess whether Metrns loss of function altered the expression patterns of *spaw*, *lft1*
173 and *lft2*, we performed *in situ* hybridization experiments for all three genes at 16 hpf (Fig. 2B).
174 At 16 hpf *spaw* is normally expressed adjacent to the KV and in the left LPM. In *metrn*$^{-/-}$ and
175 *metrnla*$^{-/-}$ single mutants as well as triplMut embryos, we could not detect any *spaw* expression
176 in the left LPM and only faintly around the KV (Fig. 2B). The spaw inhibitor *lft1* at this stage is
177 expressed along the midline. In all analyzed *metrn* mutants (single *metrn* and *metrnla* and
178 triplMut), its expression was severely disrupted at the midline (Fig. 2B, middle panel). The
179 same was observed for *lft2* which expression in the left heart field was either absent or
180 randomized in *metrn* mutants, single or triplMut embryos, compared to the wild type embryos
181 (Fig. 2B, lower panel).
182 We next characterized *dand5* specific R > L bias expression pattern in triplMut embryos by *in*
183 *situ* hybridization. In more than 61% triplMut embryos, we could detect particularly reduced
184 *dand5* expression at 14 hpf and 23% displayed an abnormal *dand5* R > L expression bias (Fig.
185 2 C-D). In single *metrn*$^{-/-}$ and *metrnla*$^{-/-}$ mutant embryos, *dand5* expression pattern was also

186 altered (Fig. S2). These results are in line with previous findings reporting that *dand5*
187 expression in the KV is only altered if upstream symmetry breaking mechanisms are disrupted
188 [37–39]. These results indicate that Metrns are required for the proper expression of Nodal
189 factor genes that are determinants of proper L-R patterning.
190
191 ***Metrns* are expressed during early zebrafish development**
192 To investigate how Metrns affect the expression of Nodal factors during early development,
193 we analyzed the pattern of expression of all three zebrafish *metrn* genes from 2 cell stage to
194 48 hpf. We first investigated the expression pattern of *metrn*, *metrnla* and *metrnlb* by *in situ*
195 hybridization and hybridization chain reaction (HCR) experiments. At the 2-cells stage, we
196 detected both *metrn* and *metrnla* maternally expressed transcripts, whereas *metrnlb*
197 expression was not detected (Fig. 3A, Fig. S3A). During gastrulation, the expression of *metrn*
198 and *metrnla* could be detected, whereas *metrnlb* expression was again not observed in our *in*
199 *situ* hybridization analysis. The earliest time point for zygotic expression of *metrn* and *metrnla*
200 was at 6 hpf (shield stage). At this stage, *metrnla* expression could be detected over the whole
201 animal cap whereas zygotic *metrn* expression onset was observed only around the yolk
202 syncytial layer (YSL) at this developmental stage (Fig. 3A). *Metrn* expression was then
203 restricted to the developing LPM and to the leading edge of the former shield area from 9 hpf
204 (Fig. 3A, Fig. S3B). In comparison, *metrnla* was found expressed throughout the whole
205 enveloping layer and developing midline (Fig. 3A, Fig. S3B). At 12 hpf, the expression of *metrn*
206 was restricted to the KV area while *metrnla* transcripts were mainly found in the midline (Fig.
207 3A-B). By 14 hpf, *metrn* expression was present in the KV area as well as in the developing
208 brain whereas *metrnla* transcripts were mainly found in the midline and the KV area (Fig. S3B).
209 In contrast, from the 2-cell stage to 14 hpf no *metrnlb* transcripts could be detected (Fig. 3A,
210 Fig. S3A-B). By HCR, we found *metrn* and *metrnla* expression colocalizing in the area of the
211 KV at 12 and 14 hpf (Fig. 3B). By 24 and 48 hpf, both genes were found strongly expressed in
212 the central nervous system (CNS) (Fig. S3C). Finally, *metrnlb* expression onset started from
213 24 hpf broadly in the embryonic brain (Fig. S3C). At 48 hpf, *metrnlb* transcripts were mostly
214 found in the otic vesicles and at the somite boundaries (Fig. S3C).
215 We next analyzed the relative expression of *metrn* genes to landmarks of the KV structure like
216 *sox32* a well-studied DFC marker [40,41]. We observed a complete colocalization of
217 *metrn*/*sox32* and *metrnla*/*sox32* signals at 10 hpf, indicating that *metrns* genes are expressed
218 in DFCs, the cells that will later form the KV (Fig. 3C-D). To assess whether *metrn* and *metrnla*
219 expression in the KV structure is conserved among vertebrates, we performed *in situ*
220 hybridization for *metrn* and *metrnla* in the chick embryo at early stages. Around stage HH6, we
221 could observe *metrn* and *metrnla* expression at the Hensen's node and around the primitive
222 streak (marked by primitive streak landmark *fgf8*) (Fig. S3D). Remarkably, the chick *metrn* and

223 *metrnla* expression patterns were reminiscent of the ones that we observed in zebrafish,
224 suggesting that *metrn* genes expression at early developmental stages in embryonic Node and
225 midline structures is conserved throughout vertebrates.
226
227 ***Metrns* loss-of-function leads to DFC disorganization and migration defects**
228 The specific expression of *metrn* and *metrnla* in DFCs and in the KV area at early
229 developmental stages led us to ask what role they may play for these cells and the KV
230 formation and function. To assess whether the loss of Metrn proteins function could affected
231 the migratory and clustering properties of DFCs, we labeled these cells in 9 hpf (80-90%
232 epiboly) gastrulating mutant embryos using the DFC landmarks *sox32* [40,41], *tbxta* [42] or
233 *sox17* [40]. Compared to wild type embryos displaying ovoid DFC clustering, about 65% of the
234 triplMut embryos displayed multiple segregated DFC clusters or abnormal linear cellular
235 distributions as shown using *sox32* marker in 9 and 10 hpf triplMut embryos (Fig. 4A-B, Fig.
236 S4B, Table 2). Similarly, *metrn*$^{-/-}$ as well as *metrnla*$^{-/-}$ single mutant embryos presented
237 clustering defects of *sox32*-expressing DFC compared to wild type embryos (Fig. 4B, Fig. S4A-
238 B, Table 2). In single or triplMut$^{+/-}$ heterozygous embryos, the DFC clustering was instead not
239 significantly or very mildly affected as revealed (Fig. S4B, Table 2). The observed defects were
240 also present when using *tbxta* and *sox17* as DFC markers whose expression was detected at
241 8 and 10 hpf respectively, indicating that although disorganized, the DFCs identity was not
242 altered by the absence of *metrns* expression (Fig. S4C). Together, these results indicate that
243 Metrns are required for the proper clustering of DFCs.
244
245 It was reported that proper adherent cell assembly is crucial for DFCs directional collective cell
246 migration during their animal to vegetal pole (AP to VP) journey [43] (Fig. 4C). We therefore
247 evaluated the migration capacity of DFCs during early development in the absence of Metrn
248 proteins. To do so, we first labeled *sox32*-expressing DFCs by *in situ* hybridization in wild type
249 and triplMut embryos and measured the position of *sox32*-expressing DFCs along the AP-VP
250 axis divided by the total embryo length at 6 hpf, 8 hpf and 10 hpf. Compared to wild type
251 embryos, DFCs in triplMut embryos showed migratory delays of about 8% to 13% at all
252 analyzed developmental stages (Fig. S5B-C, Table 3). By live imaging, we tracked the *in vivo*
253 migration of *sox17*:GFP-labeled DFCs both in triplMut and wild type embryos from 50% epiboly
254 to 90% epiboly (from 6 hpf) (Fig. 4D, Fig. S5D, Video S1-2). In line with the DFC clustering
255 abnormalities in fixed triplMut embryos that we observed, the tracking of these cells in triplMut
256 embryos *versus* wild type control embryos revealed a diminished convergence rate for triplMut
257 DFCs (Fig. 4E, upper panel). Furthermore, we measured a significant decrease of their
258 migration speed compared to the wild type DFCs (Fig. 4E, lower panel). Intriguingly,
259 individually tracked DFCs exhibited a consistent movement toward the vegetal pole, regardless

260 of the absence of Metrns proteins (Fig. 4D, Fig. S5D, Video S1-2). Taken together, these
261 findings indicate that the absence of Metrn proteins does not affect DFC migration directionality
262 but alters instead their migratory abilities including migration speed and convergence rate.
263 It was shown that during the process of epiboly, initial EVL cells destined to develop into DFCs
264 exhibit an accumulation of ZO-1 along their apical junctions. Subsequently, their apical surface
265 gradually diminishes in size, resulting in the formation of discrete apical domains enriched with
266 ZO-1 [22,24]. DFCs as such originate from dorsal EVL cells through a mechanism involving
267 the delamination of epithelial cells, facilitated by apical constriction. We asked whether the
268 observed DFC organization and migration disruptions in the absence of Meteorin proteins
269 might be attributed to perturbations in both ZO-1 accumulation and apical constriction
270 disruption. To explore this hypothesis, we examined the spatial arrangement of these regions
271 enriched with ZO-1 in triplMut embryos and WT controls during epiboly at 6 hpf and 8 hpf. As
272 expected, immunohistochemistry against ZO-1 on 6 and 8 hpf *Tg*(*sox17:GFP*) wild type control
273 embryos where DFCs are labeled with GFP were enriched in ZO-1 at their apical side and
274 apical junctions (Fig. 4F-G, Fig. S5E). At this same developmental stage, a reduced ZO-1
275 enrichment at the apical junctions of triplMut GFP-positive DFCs could be detected (Fig. 4F,
276 Fig. S5E left plot). Similarly at 8 hpf, GFP-positive triplMut DFCs exhibited diminished ZO-1 at
277 their apical region (Fig. 4G, Sy Fig. 5E right plot). Furthermore, compared to wild type DFCs,
278 triplMut GFP-positive DFCs appear to have lost their apical attachments to the EVL (Fig. 4F-
279 G, right panels). Indeed, the distance measured between triplMut DFCs and the EVL/YSL at 6
280 and 8 hpf was significantly higher compared to the one of wild type DFCs (6 hpf: **p*-value:
281 0.039, N = 4 WT, 30 DFCs measured, triplMut N = 6, 46 DFCs measured; 8 hpf: **p*-value:
282 0.021, N = 7 WT embryos, 47 DFCs measured, N = 7 triplMut, 54 DFCs measured; Fig. S5F).
283 Together, our results demonstrate that triplMut DFCs migrate significantly slower and
284 convergence less compared to wild type DFCs. Furthermore, in the absence of Metrns, DFCs
285 loose apical ZO1-enrichment and attachment to the EVL/YSL, indicating that Metrn proteins
286 are important for proper DFC clustering, migration along the AP-VP axis and their loss affect
287 ZO-1 accumulation for the connection to the EVL/YSL.
288
289 ***Metrns* loss-of-function impairs the KV formation and function**
290 At the end of gastrulation, DFCs that migrated to deeper layers of the developing zebrafish
291 embryo form a lumen to shape the KV, a ciliated organ transiently present (from around 10.5
292 hpf to 30 hpf [44]) that is crucial for initiating L-R asymmetric patterning [9,23]. As we observed
293 at 14 hpf, it was reported that Dand5, a member of Cerberus/Dan family of secreted factors, is
294 expressed adjacent to the KV with a right – left (R > L) bias between 11 and 14 hpf in zebrafish
295 (Fig. 2) [45]. The right-biased expression of *dand5* was shown to be directly influenced by the
296 direction and the strength of the Nodal flow generated by the KV [46]. In return, Dand5

297 contributes to the left-biased expression of *spaw* in the LPM by antagonizing Spaw activity
298 [45]. The leftward-directed flow generated by the KV was also shown to be important for the
299 asymmetric expression of other Nodal genes, like *spaw*, *lefty1* (*lft1*) and *lefty2* (*lft2*) [26,27].
300 The observed disturbed expression of these Nodal factors in the absence of Metrns led us to
301 hypothesize that Metrn proteins might not only be critical for the proper clustering and migration
302 of DFCs but also for the proper formation and function of the KV. To assess this question, we
303 first labeled the cilia present in the KV of wild type and triplMut embryos at 14 hpf by anti-
304 acetylated tubulin immunostaining (Fig. 5A). We then measured the number of cells in the KV,
305 the KV diameter and the number of cilia, which were correlating with the number of cells, of
306 both wild type and triplMut embryos (Fig. 5B-D). Previous work has shown that the KV diameter
307 and the number of KV cilia cells as well as KV cilia can be highly variable from embryo to
308 embryo [47]. Nevertheless, despite the wide variability, we observed highly significant
309 reduction in all cases (Fig. 5B-D). In addition, compared to the wild type controls, triplMut
310 embryos also displayed a significant reduction in the KV cilia length (Fig. 5E).
311 Furthermore, we investigated both the KV lumen and the process of DFC-to-KV organization.
312 As described recently and observed in ZO-1 stained embryos, by 14 hpf DFCs clustering into
313 a rosette structure lead tight junctions to form the KV lumen [22] (Fig. S6A, left panel). In
314 contrast, ZO-1 immunostained triplMut embryos of the same developmental stage displayed
315 an irregular ZO-1 lattice pattern and disrupted KV lumen shape (Fig. S6A, right panel).
316 Additionally, unlike in control embryos, triplMut embryos displayed only partially polarized
317 DFCs indicated by absent or irregular aPKC-ζ immunolabeling (Fig. S6B). These results
318 indicate that the loss of Metrns function also impacts the proper DFC polarization and
319 subsequent KV formation.
320
321 We next evaluated whether the deficient formation of the lumen as well as the reduced number
322 and cilia length in triplMut altered the KV function. To do so, we compared the Nodal flow
323 generated by the KV of triplMut embryos to the one of wild type embryos. The movement
324 generated by the KV cilia was monitored by injecting fluorescent microspheres (0.5 μm) into
325 the KV at 12-14 hpf. To quantify the flow inside the KV, fluorescent microbeads movement was
326 tracked in WT control (n = 363 beads in 4 embryos) and in triplMut embryos (n = 318 beads in
327 4 embryos) (Fig. 5F). Beads movement analysis within the KV showed a counter-clockwise
328 rotation of the flow in wild type control (Fig. 5F, Video S3). In contrast, this movement was
329 severely impaired in triplMut embryos (Fig. 5F, Video S4). To quantify the properties of the
330 beads displacement, we computed the mean square displacement (MSD), which enables to
331 distingue between directed and confined motion. This analysis revealed a directed motion of
332 microbeads in the wild type KV (MSD quadratic dependence on Δt) and a confined motion
333 (MSD asymptotic behavior) in triplMut [48]. Accordingly, measurement of average bead

334 velocity showed an overall reduction in the beads speed in the triplMut mutant embryos
335 compared to the wild types (WT mean = 0.96212 µm/sec; TriplMut mean = 0,47996 µm/sec;
336 Fig. S6C). These results demonstrate that the observed defects in the KV formation in the
337 absence of Metrns also severely impacts its function and thereby the Nodal flow generation,
338 responsible for proper Nodal factors expression.
339
340 **Genetic interaction of ItgαV/Itgβ1b and Metrns on the level of the DFCs**
341 In order to further uncover the mechanisms through which Metrn proteins act in the
342 establishment of early L-R patterning, we finally assessed the possible relationship between
343 Metrns and mediators of the extracellular matrix like Integrin αV1 (ItgαV1) and Integrin β1b
344 (Itgβ1b). Integrins are membrane receptors involved in cell adhesion and recognition during
345 embryogenesis amongst others [49]. During gastrulation, *itgαV* as well as *itgβ1b* were shown
346 to be expressed in DFCs and *itgαV* and *itgβ1b* morpholino-injected embryos display DFC
347 phenotypic defects reminiscent to those observed in *metrn* mutants [50].
348 We therefore asked whether Metrns loss of function could affect the expression of both
349 integrins. To do so, we quantified *itgαV* and *itgβ1b* expression levels in wild type and triplMut
350 embryos at 6, 9 and 24 hpf by qRT-PCR. No significant change in *itgαV* and *itgβ1b* expression
351 levels at either tested developmental stage was measured in triplMut embryos compared to
352 wild type controls (Fig. S7A).
353 In order to test whether ItgaV1 and Itgβ1b and Metrns genetically interact, we injected
354 insufficient doses of morpholinos for *itgβ1b* (0.5 ng) or *itgαV1* (0.41 ng) into 1 to 4 -cell stage
355 in a heterozygous *metrns* mutant background. The injection of the morpholinos at these doses
356 and at sufficient doses (*itgβ1b:* 0.7 ng, *itgαV1:* 1.25 ng) reproduced the previously reported
357 defects on DFCs (Fig. 6A, Table 4) [50]. Instead, the injection of low doses of either *itgβ1b* or
358 *itgαV1* morpholino did not affect DFC clustering, similarly to non-injected triplMut$^{+/-}$ embryos
359 (Fig. 6A, Table 4). However, a significantly higher percentage of embryos with DFC clustering
360 defects could be observed upon the injection of either morpholino at low dose into triplMut$^{+/-}$
361 (Fig. 6A, Table 4). These results are consistent with the hypothesis that Metrn proteins act
362 together with both Integrins for the proper clustering and migration of DFCs during early
363 embryonic development without directly affecting their expression.
364

365 **DISCUSSION**

366

367 Proteins of the Meteorin family were first described as secreted neurotrophic factors highly
368 conserved among vertebrates [28–31]. In mouse *Metrnla* mutants display phenotypes as
369 impaired angiogenesis after ischemic injury [51] or dysregulated cytokine production [52]. The
370 disruption of *Metrn* resulted in early embryonic lethality [28] preventing to investigate the
371 combined role of Metrn proteins in early embryonic development *in vivo* and in particular its
372 role in L-R patterning. Here, using the zebrafish larva as model system, we generated knockout
373 lines for all three zebrafish *metrn* genes, *metrn*, *metrnla* and *metrnlb*, which are all viable and
374 fertile, possibly attributed to species specific differences in compensatory mechanisms,
375 allowing for the study of Meteorins functions during early embryonic development.
376 Our results demonstrate that Metrns are required for symmetry breaking and the establishment
377 of L-R asymmetry, a novel role for Meteorin proteins during vertebrate embryonic
378 development. All three paralogs analyzed, when genetically deleted, had an effect on heart
379 looping formation, with the strongest effect for Metrnla and Metrn while Metrnlb had a smaller
380 but still significant effect. In our *in situ* analysis, we failed to detect early *metrnlb* expression.
381 We do not exclude that at early stages, *metrnlb* could be expressed at very low level or in a
382 very small number of cells that we cannot detect. However, in the *metrnlb* mutant, the loss of
383 this expression could still be sufficient to induce the low penetrant phenotype. Interestingly,
384 when analyzing the expression of these genes in a single cell transcriptomic atlas at the earliest
385 available time point (10 hpf), in contrast to the robust expression of the two first genes, *metrnlb*
386 expression is indeed found in very few cells [53].
387 We show that Metrns play a crucial role in ensuring this function the genetic interaction with
388 the integrins ItgαV1 and Itgβ1b known to facilitate the proper clustering and migration of DFCs
389 based on the sufficient accumulation of ZO-1 and apical constriction, essential to form the KV
390 [22,50]. Furthermore, our results reveal that Metrns are essential for several aspects of the KV
391 formation and function including the cilia length, cilia number, KV size and lumen formation.
392 Consequently, Metrns are important for the regulation of the proper expression of Nodal flow
393 genes and that this regulation is critical for the proper asymmetric positioning and morphology
394 of vital organs like the heart (Fig. 6B).

395

396 Previous work has shown that zebrafish midline mutants display altered *lft1* and *lft2* expression
397 patterns as well as discordance among heart, gut and brain gene expression patterns [54].
398 From 9 hpf *metrn* expression was visible around the developing LPM close to the midline and
399 the leading edge of the shield. *Metrnla* expression was found throughout the whole enveloping
400 layer and the developing midline which plays an important role in vertebrate L-R development.
401 Despite the expression of both paralog close to or at the midline, we hypothesize that the

402 described body asymmetry defects in triplMut embryos do not originate from impaired midline
403 structures but rather impaired DFC clustering and migration. Indeed, triplMut$^{-/-}$ embryos display
404 intact *tbxta*-positive notochords (Fig. S4C), as well as randomized visceral organs positioning
405 (Fig. 1D-E), phenotypes that are not characteristic for defects of the anterior midline [54].
406 DFCs are precursors of the zebrafish KV, organ of laterality, essential for the L-R axis
407 establishment. DFCs develop at the beginning of gastrulation and form the KV by the end of
408 gastrulation [9,23]. Given the early onset of *metrn* and *metrnla* expression and their specific
409 expression within the DFCs, we investigated their role for the clustering and migration capacity
410 of DFCs during these early embryonic developmental steps. In the course of their migration,
411 DFC progenitors intercalate mediolaterally and results in an oval-rosette shape cluster of DFCs
412 by mid-gastrulation that will form the KV [22]. *Metrn*$^{-/-}$*, metrnla*$^{-/-}$ and triplMut zebrafish embryos
413 displayed DFC assembly defects and delayed migration of these cells during gastrulation.
414 Since DFCs in triplMut still express DFC specific markers (*sox17, sox32, tbxta*), we concluded
415 that Metrns are not required for the specification of DFCs *per se* but rather that Metrns are
416 important for their proper clustering and migration.
417
418 It is important to note that the observed DFC clustering and migration abnormalities in Metrn
419 mutants primarily affect the apico-ventral axis rather than the mediolateral axis. This is evident
420 from the disrupted connection between DFCs and the YSL/EVL in these mutants, while the
421 migration directionality remains intact. Since a proper connection between DFCs and the EVL
422 facilitates a subset of DFCs to establish apical contacts with the EVL and become pre-
423 polarized, one could speculate that Metrns are involved in the polarization and establishment
424 of direct apical contacts of DFCs with the EVL [22–24,55]. This disrupted connection in *metrns*
425 loss-of-function embryos, which usually links DFCs with the vegetal spread of extra-embryonic
426 tissues [24], likely results in the observed DFCs vegetal motion defects.
427 It has been demonstrated that these apical attachments function as tissue connectors, linking
428 DFCs with the spreading of extra-embryonic tissues towards the vegetal pole [24].
429 Therefore, the loss of apical attachments in the mutant embryos causes all DFCs to converge
430 less and migrate more slowly than in wild-type controls, as shown by our *in vivo* imaging
431 analysis.
432 This would imply that a number of DFCs was simply too slow to reach the vegetal pole in time
433 to form a fully functional KV. Given that KV cilia are monocilia, this subsequently results in a
434 diminished count of KV cells (Fig. S5A), along with the observed structural abnormalities in the
435 KV lumen and impairments in its overall functionality.
436 Additionally it was shown that the formation of the developing KV lumen was directly connected
437 to ciliogenesis as polarized DFCs initiate developing cilia at their membrane domain facing the
438 forming lumen [22]. This indicates that proper DFC polarization is essential for the KV

439 formation and for ciliogenesis. In *metrns* mutants the reduced cilia length and the lack of PKCζ
440 staining in the developing KV further highlights an impairment of DFC polarization in the
441 absence of Metrns consequently leading to KV formation and function defects. Further work
442 would be needed to explore whether Metrns directly impact the motility of KV cilia or if the
443 disrupted Nodal flow observed is solely caused by the disturbed KV lumen.
444
445 It has been demonstrated that an appropriate asymmetrical Nodal flow plays a crucial role in
446 the asymmetrical expression of Nodal genes such as *dand5, spaw, lefty1 (lft1),* and *lefty2 (lft2)*
447 [26,27,45]. As such, the disrupted formation and function of the KV in *metrns* mutants might
448 contribute to the evident perturbation in Nodal factor expression and may also induce
449 randomization of Nodal factor expression in L-R asymmetry [9,15,47,50]. We do not exclude
450 however that Metrns directly impact the expression of *spaw, leftys* and *dand5* in addition to
451 their role in DFC cell behaviors and KV formation. One of the earliest functions attributed to
452 Meteorin was as a regulator of mesendoderm development through the enhancement of nodal
453 expression [28]. In this context, several studies have reported that Nodal signaling was shown
454 to regulate DFC specification [56,57].
455 In line with the impaired KV formation and function that we observed in *metrns* mutants, it was
456 shown that knockdown of Integrin αV as well as Integrin β1b in zebrafish results in L-R
457 asymmetry defects [50]. This was explained by DFC organization and migration defects and
458 disturbed KV formation. Integrin αVβ1 specific functions have not yet been completely resolved
459 in mammals, mostly due to their broad expression and redundant function with other integrins,
460 as well as the lack of antibodies and inhibitors specific for αVβ1. However, several *in vitro*
461 studies have already connected αVβ1 to developmental processes. For instance, αVβ1 was
462 shown to be implicated in embryonic astrocytes and oligodendrocyte precursors migration in
463 rodents [58] and neural cell adhesion molecule L1 cell binding [59]. Additionally, the fibronectin
464 receptor integrin α5β1 has been found to be crucial for regulating extracellular matrix assembly
465 along tissue boundaries, in coordination with Eph/Ephrin signaling [60].
466 Our results suggest that one mechanism by which Metrns act is through their genetic
467 interaction with Integrin αV/β1b to mediate the proper clustering of DFCs. These interactions
468 could influence Integrin's adhesive functions (or other properties) necessary for DFC
469 clustering. If so, the absence of Meteorins would lead to disturbed adhesion and/or Integrin
470 signaling, resulting in DFC migration defects and disturbed KV development. Interestingly, it
471 was shown that in αV and β1b morphants DFC-EVL connections remain intact [50], unlike in
472 our *meteorin* mutants. This contrast suggests that Meteorins alone are crucial for DFC
473 polarization and that their interaction with integrins αVβ1b may rather be important for the
474 subsequent steps leading to KV formation. While our genetic interaction studies provide strong

475 evidence of a link between Meteorins and Integrins, further biochemical analyses are required
476 to fully elucidate this interaction.
477 Despite the recent advancements in uncovering the multiple functions of Meteorins, their
478 receptors during early development are still unknown. It was recently shown that METRNL is
479 promoting heart repair through its binding to the KIT tyrosine kinase receptor, establishing
480 METRNL as a KIT receptor ligand in the context of ischemic tissue repair [51]. In another study,
481 it was reported that Metrn is a ligand for the 5-hydroxytryptamine receptor 2b (Htr2b) [61].
482 Additionally Metrn was associated with the regulation of reactive oxygen species levels in
483 hematopoietic stem/progenitor cells via directing phospholipase C signaling [61]. When we
484 analyzed the expression of *kita*, one of the two zebrafish orthologs to KIT tyrosine kinase
485 receptor, at 9 hpf we found that *kita* is solely expressed in the prechordal plate and later (from
486 11 hpf) in the lateral borders of the anterior neural plate (Fig. S7B, left panel). Its paralog *kitb*
487 is expressed from 11 hpf in the anterior ventral mesoderm (Fig. S7B, right panel), as previously
488 reported [62]. Additionally, the analysis of *htr2b* expression during zebrafish development
489 revealed that its expression only starts from around 2 dpf in the heart (Fig. S7C). The absence
490 of *kita/b* as well as *htr2b* expression at early embryonic stages in or at proximity of DFCs and
491 in the forming KV suggests that Metrns rather act through other receptor(s) to ensure their L-
492 R patterning functions.
493
494 Mechanisms underlying L-R patterning are known to be highly conserved within vertebrates.
495 Hence, we raised the question whether Meteorin protein family is conserved across different
496 species. Genes coding for *metrn* and *metrnl* exist in several vertebrates classes but could not
497 be found in the genomes of invertebrates [63]. *Metrnl* orthologs genes could instead be found
498 in amphioxus and tunicates. Therefore, we propose that Metrns function in the establishment
499 of the L-R axis that we have uncovered here emerged during Chordate evolution (Fig. S7D).
500

501 **MATERIAL AND METHODS**

502

503 **Zebrafish husbandry**

504 Zebrafish (*Danio rerio*) were maintained at 28°C overnight (O/N) at 14 hours light/10 hours
505 dark cycle. Fish were housed in the animal facility of our laboratory which was built according
506 to the respective local animal welfare standards. All animal procedures were performed in
507 accordance with French and European Union animal welfare guidelines with protocols
508 approved by the committee on ethics of animal experimentation of Sorbonne Université
509 (APAFIS#21323- 2019062416186982). For all experiments in this study, primarily zebrafish
510 AB strains were used unless stated otherwise. The *Tg*(*sox17:GFP*) lines were created via
511 injection of a *pTol2-sox17:GFP* plasmid (kindly gifted from Didier Stanier and Stephanie Woo)
512 into one-cell stage zebrafish embryos together with 150 ng/ml of *tol2* mRNA. Injected embryos
513 were grown to adulthood and screened for GFP in their offspring.

514

515 ***Metrn*, *metrnla* and *metrnlb* CRISPR-Cas9-mediated mutagenesis**

516 SgRNA guide sequences were cloned into a BsaI-digested DR274 plasmid vector (Addgene
517 42250). The sgRNAs were synthesized by *in vitro* transcription using (using the Megascript T7
518 transcription kit, Ambion, AM1334). After transcription, sgRNAs were purified using a RNAeasy
519 Mini Kit (Qiagen). The quality of purified sgRNAs was checked by electrophoresis on a 2 %
520 agarose gel. The target sequences were the following:

521

	Sequence (5' - 3')
metrn	CCACCACACCCGGCCCAGCC
metrnla	GGTGTATCTCCGCTGCGCCC
metrnlb	CCAGAAACAGCGCCCCCTCC

522

523 *Cas9* mRNA was generated as described in Hwang, Fu et al. 2013 [64]. To induce targeted
524 mutagenesis at the *metrn, metrnla* and *metrnlb* loci, 200 ng/ml of sgRNA were injected into
525 one-cell stage zebrafish embryos together with 150 ng/ml of *cas9* mRNA. Injected embryos
526 were grown to adulthood and screened for mutation in their offspring.

527

528 **DNA extraction and sequencing for analysis of CRISPR/Cas9- mediated mutagenesis**

529 For genomic DNA extraction, pools of 5 dpf embryos were digested for 1 h at 55 °C in 0.5 mL
530 lysis buffer (10 mM Tris, pH 8.0, 10 mM NaCl, 10 mM EDTA, and 2% SDS) with proteinase K
531 (0.17 mg/mL, Roche Diagnostics) and inactivated 10 min at 95 °C. To check for frequency of
532 indel mutations, target genomic loci were PCR amplified using a Phusion High-Fidelity DNA
533 polymerase (Invitrogen). PCR amplicons were subsequently cloned into a *pCR-bluntII-TOPO*

534 vector (Thermo Fisher). Plasmid DNA was isolated from single colonies and Sanger
535 sequencing was performed by Eurofins. Mutant alleles were identified by comparison with the
536 wild type sequence using Geneious software.
537
538 **Mutants genotyping and generation of triple mutants**
539 Genotyping of *metrns* mutants was performed as follows: after genomic DNA extraction PCR
540 amplification reactions were conducted in final volumes of 20 µl containing 1x PCR reaction
541 buffer, 1,5mM MgCl2, 70 ng of gDNA, Taq DNA Polymerase (5U/µl) and 0.5 µM of each primer.
542

	Sequence (5' - 3')
***metrn*-fw**	CTGTGTTGACTGCTGGCTG
***metrn*-rv**	GTGGTTTAGTGGTGTTCTTACAATGA
***metrnla*-fw**	TCCCATGCCTGGACCTCATA
***metrnla*-rv**	AGACGGAGAGAAGAGACGCT
***metrnlb*-fw**	TGTTGATCAGCAGTGTGTGCGTAGC
***metrnlb*-rv**	GTCCTCCGCTGATCTACGTG

543
544 The DNA amplification was performed with 35 cycles at the annealing temperature of 60°C.
545 *Metrn* and *metrnlb* amplicons were loaded on 2 % agarose gel to discriminate between wild
546 type and mutant alleles (for *metrn*, the expected size of wild type amplicon is 598 bp while the
547 mutant amplicon is 482 bp long using the same primer set; for *metrnlb*, the size of the expected
548 wild type amplicon is 242 bp while the mutant band is 156 bp long using the same primer set).
549 *Metrnla* PCR product was digested at 55°C O/N with the PasI restriction enzyme and the
550 resulting digestion was subsequently analyzed on a 2% agarose gel. The wild type amplicon
551 results in two fragments of 107 bp and 94 bp length, respectively. The mutant amplicon band
552 size is instead 201 bp using the same primer set. Triple mutants were obtained first by
553 incrossing homozygous *metrn* and *metrnla* mutants to generate double heterozygous mutants.
554 Double heterozygous mutants were then crossed with homozygous *metrnlb*$^{-/-}$ fish and
555 genotyped to identify triplMut$^{+/-}$ triple heterozygous mutants. triplMut$^{+/-}$ fish were incrossed and
556 genotyped to identify triplMut$^{-/-}$ triple homozygous mutants. In all described experiments of this
557 study, triplMut$^{+/-}$ were obtained by outcrossing female triplMut$^{-/-}$ fish with male wild type fish, if
558 not stated differently to prevent from *metrns* maternal contribution.
559
560 **Hybridization chain reaction (HCR)**
561 All HCR probes and solutions were purchased from Molecular Instruments®. Dechorionated
562 embryos at the developmental stage(s) of interest were fixed in 4% paraformaldehyde in PBS
563 (pH 7.4) for 2 hours at room temperature, followed by several washes with PBS to stop the

564 fixation. Embryos were then dehydrated with a series of methanol (MeOH) washes and stored
565 at -20°C. The HCR was performed following the manufacturer's instructions. HCR samples
566 were imaged on an inverted confocal microscope Olympus FV-1000, employing a 20x oil
567 immersion objective (NA 0.85). Z-volumes were acquired with a 5 µm resolution and images
568 were processed and analyzed using ImageJ.
569
570 ***In situ* hybridization in zebrafish and chicken**
571 The respective cDNA fragments were amplified by PCR from total zebrafish or chicken cDNA
572 of stage 12 hpf – 48 hpf and HH6. *In vitro* transcription of Digoxigenin/Fluorescent-labeled
573 probes was performed using an RNA Labeling Kit (Roche Diagnostics Corporation) according
574 to manufacturer's instructions. Zebrafish and chicken whole-mount *in situ* hybridizations were
575 performed as previously described [65] [66]. Stained embryos were then imaged on a Leica
576 MZ10F stereomicroscope. Images were processed and analyzed using ImageJ software.
577 Color balance, brightness and contrast were applied uniformly. Fluorescently-labeled samples
578 were imaged using an inverted confocal microscope Olympus FV-1000, employing a 40x oil
579 immersion objective (NA 1.30). Z-volumes were acquired with a 0.5 µm resolution and images
580 were processed and analyzed using ImageJ.
581
582 **Analysis of DFC phenotype and migration**
583 For the DCF clustering analysis, Bayesian inference was used to recover the maximum-
584 likelihood value for the malformation probability. The outcome of an experiment was
585 considered to be a binary random variable (malformed or wild type phenotype) whose
586 probability depends solely on the experimental condition. The total number of malformed
587 phenotypes per experiment is therefore binomially distributed. The posterior distribution is
588 obtained by inverting this binomial distribution using Bayes theorem, under a uniform prior.
589 Under these hypotheses the maximum-likelihood estimate for the malformation probability is
590 simply given by the empirical malformation frequency. The standard deviation of the posterior
591 distribution was used to provide a confidence interval for the estimate (black error bars). *P*-
592 values were evaluated using Fisher exact test on the number of malformed and wild type
593 phenotypes. AP to VP DFC migration was calculated as the percentage of the total embryo
594 length.
595 For *in vivo* live DFC imaging, a *pEGFP-sox17* construct (Addgene #31400) and *H2B-RFP*
596 mRNA were co-injected either in wild type or triplMut embryos that were embedded at 50%
597 epiboly (6 hpf) in 1% low melting-point agarose diluted in E3 water. DFC were identified as
598 recently described in [24]. Imaging was performed in a temperature constant environment with
599 a 10x water dipping objective using an upright Yokogawa CSU-X1 spinning disk scan head,
600 mounted on a DM6000 upright Leica microscope and a CCD CoolSnap HQ2 camera at 4 Hz.

601 Volumetric image stacks were acquired every 6 minutes which was sufficient to manually track
602 individual DFC migration during 3 hours from 50% epiboly. No drift correction was required.
603 The convergence ratio was calculated by comparing how far the tracked cells stretched along
604 the y-axis at the beginning and end of each recording (as visualized in Fig. 4D and described
605 in Pulgar et al., 2021 [67]).
606
607 **qRT-PCR and analysis**
608 For gene expression analysis, total RNA extraction was prepared from zebrafish embryos with
609 TRIzol reagent (Thermo Fisher) and TURBO DNA-free reagents (Invitrogen™ AM1907M).
610 Total RNA was cleaned up using RNeasy Mini Kit (Qiagen) following the manufacturer's
611 instructions and treated twice with DNase I (1 U/µg RNA, Qiagen). The RNA concentration
612 was quantified using the Nanodrop2000 (Thermo Fisher). RNA (1 µg) was retro-transcribed
613 using random primers and a SuperScript III First-Strand Synthesis system (Invitrogen
614 18080051). For qRT-PCR, the SYBR Green PCR Master Mix (Thermo Fisher) was used
615 according to the manufacturer's protocol. *Ef1a* was used as reference genes as previously
616 reported [68]. All assays were performed in triplicates and repeated in 3 independent
617 experiments. The mean values of triplicate experiments were calculated according to the delta
618 CT quantification method [69] and a student T-test was applied for the *p*-value calculation.
619
620 **mRNA synthesis and injection**
621 Zebrafish *metrn* and *metrnla* cDNA fragments were amplified by PCR from zebrafish cDNA of
622 1 dpf. The fragments were cloned into a *pCS2+* plasmid linearized with Xho1 and Xba1
623 restriction enzymes using a Quick Ligation Kit (NEB). The *pCS2:h2b-rfp* plasmid readily
624 available in the laboratory was linearized with the NotI restriction enzyme and the mRNA
625 synthesis was performed by *in vitro* transcription using the mMESSAGE mMACHINE Sp6 Ultra
626 kit (AM1340, Ambion) adding 1 µL of GTP as recommended by the manufacturer's instructions
627 and followed by lithium chloride precipitation. 150 ng.µL^{-1} of the synthesized mRNA was then
628 injected into 1- to 4-cell-stage zebrafish embryos.
629
630 **Design and injection of antisense morpholino oligonucleotides**
631 The published morpholinos (MO) used in this study for *itgαV* (5'-
632 AGTGTTTGCCCATGTTTTGAGTCTC-3'), *itgβ1b1* (5'-GGAGCAGCCTTACGTCCATCTT
633 AAC-3') and for control (ctrl MO) (5'-CCTCTTACCTCAGTTACAATTTATA-3') were injected
634 using the same reported concentration of 0.41 ng (*itgαV*) and 0.5 ng (*itgβ1b1*) for insufficient
635 doses, 1.25 ng (*itgαV*) and 0.7 ng (*itgβ1b1*) for full knock down effect and 2.5 ng for the ctrl

636 MO [50]. All MOs were obtained from Gene Tools (Philomath, OR, USA). MOs were injected
637 in 1 to 4 -cells stage zebrafish embryos.
638
639 **Whole-mount immunohistochemistry**
640 Embryos were fixed in 4% paraformaldehyde in PBS-Tween for 2h at room temperature (RT)
641 and subsequently washed three times in PBS-1% Triton X-100 to promote their
642 permeabilization. They were then incubated for 1 hour at RT in blocking solution (10% Normal
643 Goat Serum, in PBS-Tween) followed by overnight incubation, at 4°C with primary antibodies
644 diluted at 1:200 in 1% blocking solution. The following primary antibodies were used: anti-
645 acetylated tubulin (Sigma T6793); anti-ZO1 (339100, Invitrogen, Carlsbad, CA, USA); anti-
646 GFP (GTX13970, GeneTex); anti-aPKCζ (sc-216, Santa Cruz Biotechnology Inc., CA, USA).
647 After five washes in 1x PBS-Tween, the embryos were then incubated O/N with respective
648 Alexa Fluor IgG secondary antibody (Life Technologies) diluted 1:200 in 1% blocking solution.
649 The following day embryos were washed five times in 1x PBS-Tween and mounted in 1% low-
650 melting point agarose in glass-bottom cell tissue culture dish (Fluorodish, World Precision
651 Instruments, USA). An inverted confocal microscope Olympus FV-1000 was used for imaging,
652 employing a 20x objective (NA 0.75) or a 40x oil immersion objective (NA 1.30). Z-volumes
653 were acquired with a 0.5 µm resolution and images were processed and analyzed using
654 ImageJ and Imaris. The distances between the DFCs and the EVL at 6 and 8 hpf were
655 measured in fixed whole-mount samples. Using ImageJ, the distances were analyzed from the
656 center of the leading DFCs to the leading edge of the EVL, as marked by ZO-1. The area of
657 ZO-1 enrichments was measured using Fiji in cropped images that included only DFCs and at
658 6 hpf also the apical part of the EVL.
659
660 **Fluorescent microspheres injection and analysis**
661 FluoSpheresH fluorescent microspheres injection was conducted as previously described [70].
662 Embryos were embedded in 1% low melting-point agarose diluted in egg water. Imaging was
663 performed with a 40x water dipping objective using an upright Yokogawa CSU-X1 spinning
664 disk scan head, mounted on a DM6000 upright Leica microscope and a CCD CoolSnap HQ2
665 camera at 4 Hz using the green channel at 0.25 µm resolution on a single Z-plane. Beads
666 trajectory tracking was performed using an already developed toolbox [71]. The size detection
667 parameter was set to 0.75 – 1.25 µm objects with a brightness superior to the 0.01 percentile
668 of the whole image. Objects that traveled less than 2.5 µm between two consecutive frames
669 were linked into the same trajectory and considered as a single bead. Objects traveling longer
670 distances were analyzed as separate trajectories, even if they originated from the same bead.
671 Analyses were then performed using a custom-made Matlab code. For better visualization,
672 trajectory plots only show 20 tracked beads. MSD analysis was conducted using an already

673 published code (https://tinevez.github.io/msdanalyzer/) [72]. Average mean square
674 displacement (MSD) plots only show particles tracked between 1 and 8 seconds. Very short
675 tracking durations do not permit to correctly estimate displacement properties and less than
676 1% of the particles were tracked for more than 8 seconds.
677
678 **Data analysis**
679 Expression analysis, DFC clustering, and heart and visceral organ positioning experiments
680 were conducted at least three independent times, each with a comparable N number, to ensure
681 reproducibility and account for batch effects. The reported data represent pooled results from
682 these independent experiments. Experiments for heart looping, *dand5* expression and visceral
683 organ phenotypes have multinomial outcomes, and the *p*-values for these distributions were
684 evaluated accordingly. For any given pair of conditions α (control) and β (mutated condition),
685 the number of observed experimental outcomes were counted. The number of outcomes for
686 each condition was denoted as (nα, dα, rα) and (nβ, dβ, rβ), with Nα and Nβ denoting the total
687 number of observations. The frequency of each outcome under a particular condition is simply
688 the number of observations for the given outcome divided by the total number of observations.
689 The dissimilarity between two conditions α and β was measured as the sum of absolute
690 differences between their respective frequencies $\delta = |fn\alpha - fn\beta| + |fd\alpha - fd\beta| + |fr\alpha - fr\beta|$. Then
691 the probability of the null hypothesis was estimated, i.e., that the multinomial distributions of
692 outcomes related to the two conditions are the same, as the probability of obtaining a
693 dissimilarity equal or higher to the one observed by simply pooling all the observations
694 together, and again randomly subdivided in two sets of observations of size Nα and Nβ. To
695 numerically estimate this probability the procedure of pooling the observations together was
696 repeated for K = 100'000 times, randomly separating them again in two sets, and evaluating
697 the new dissimilarity δ'. The probability of the null hypothesis is then given by the numerical
698 frequency with which the dissimilarity $\delta' \geq \delta$ is greater or equal to the one observed in the
699 experiments. [73,74]
700 Python and Matlab codes used for beads and DFC tracking are available at
701 https://github.com/jboulanger91/meteorin. Codes for statistical analysis are available at
702 https://github.com/FannyEggeler/Meteorin_analysis.
703
704 **Phylogenetic analysis**
705 Protein sequences were obtained from the Ensembl Genome Browser or UniProt. The
706 following sequences were used: *D. rerio* Metrn (ENSDARP00000041804.5), *D. rerio* Metrnla
707 (ENSDARP00000131064.1), *D. rerio* Metrnlb (ENSDARP00000126894.1), *G. gallus* Metrn
708 (ENSGALP00010026416.1), *G. gallus* Metrnl (ENSGALP00010044844.1), *H. sapiens* Metrn
709 (ENSP00000455068.1), *H. sapiens* Metrnl (ENSP00000315731.6), *M. musculus* Metrn

710 (ENSMUSP00000127275.2), *M. musculus* Metrnl (ENSMUSP00000038126.8), *X. leavis*
711 Metrnl (ENSXETP00000107425.1), *L. oculatus* Metrn (ENSLOCP00000003703.1), *L. oculatus*
712 Metrnl (ENSLOCP00000017224.1), *B. lanceolatum* (A0A8K0F3K3), *S. clava*
713 (XP_039261436). *L. oculatus* was chosen as an outgroup, *B. lanceolatum* as an example for
714 Cephalochordata and *S. clava* as a representative for Tunicata. The phylogenetic tree was
715 reconstructed with the phylogeny analysis from www. phylogenie.fr [75–81].
716

717 **FIGURE LEGENDS**

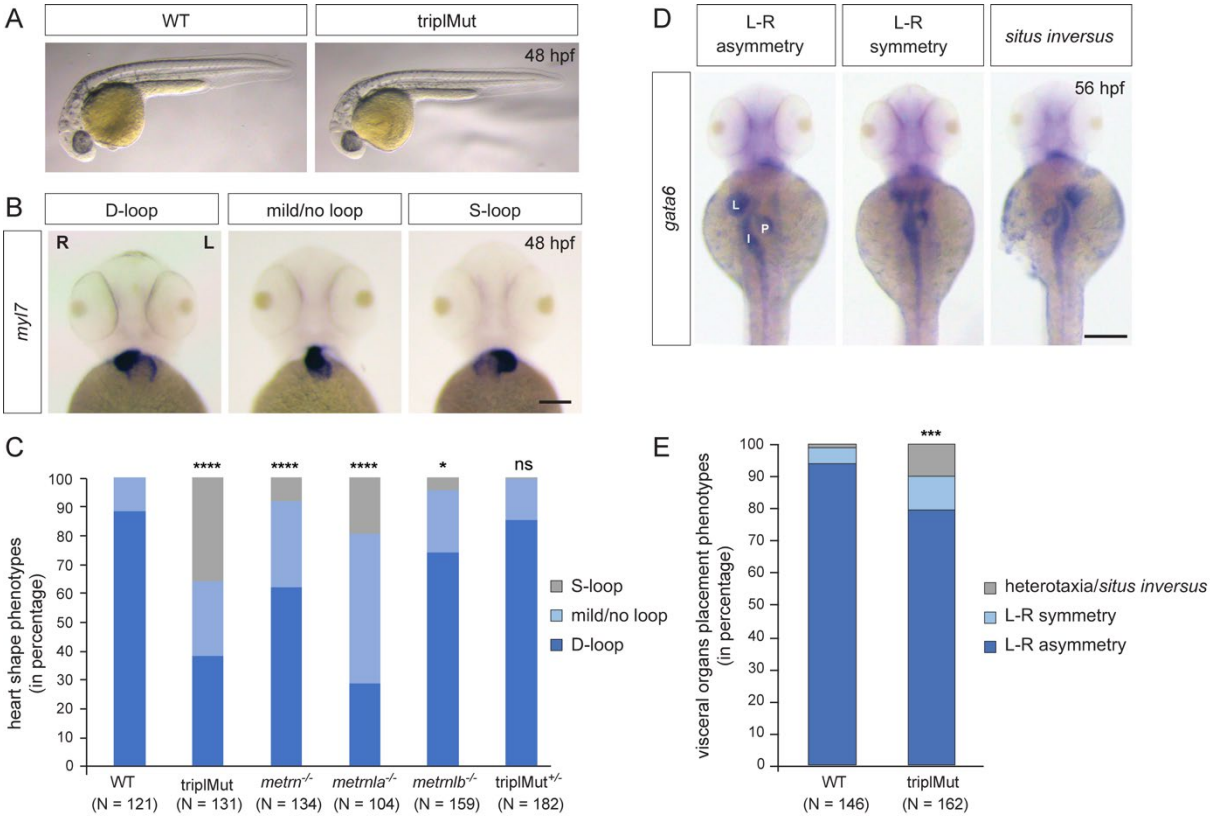

718 Figure 1

Fig. 1. Metrns loss-of-function causes heart jogging/looping and visceral organ positioning defects. (**A**) 48 hpf triplMut zebrafish display no gross phenotypic defects compared to wild type (WT) embryos. (**B**) Examples of 48 hpf embryos showing mRNA expression of the heart marker *myl7* and the different heart looping phenotypes (ventral view). (**C**) Quantification in percentage of heart looping phenotypes at 48 hpf in WT, triplMut, *metrn*$^{-/-}$, *metrnla*$^{-/-}$, *metrnlb*$^{-/-}$, triplMut$^{+/-}$ embryos; displayed *p*-values compared to WT: ****p-value: <1.0e-5 for triplMut, ****p-value: <1.0e-5 for *metrn*$^{-/-}$, ****p-value: <1.0e-5 for *metrnla*$^{-/-}$, *p-value: 0.003 for *metrnlb*$^{-/-}$, ns p-value: 0.49 for triplMut$^{+/-}$, p-value compared to *metrnlb*$^{-/-}$: *p-value: 0.034 for triplMut$^{+/-}$ (not displayed). (**D**) Example of 56 hpf embryos showing *gata6* mRNA expression highlighting the different visceral organ positioning phenotypes (ventral view). (**E**) Quantification in percentage of visceral organ positioning phenotypes at 56 hpf in WT and triplMut embryos, ***p-value: 0.00034. In (B) L = left, R = right. In (D) L = liver, P = pancreas, I = intestine. Scale bars in (**B**): 100 µm, (**D**): 500 µm.

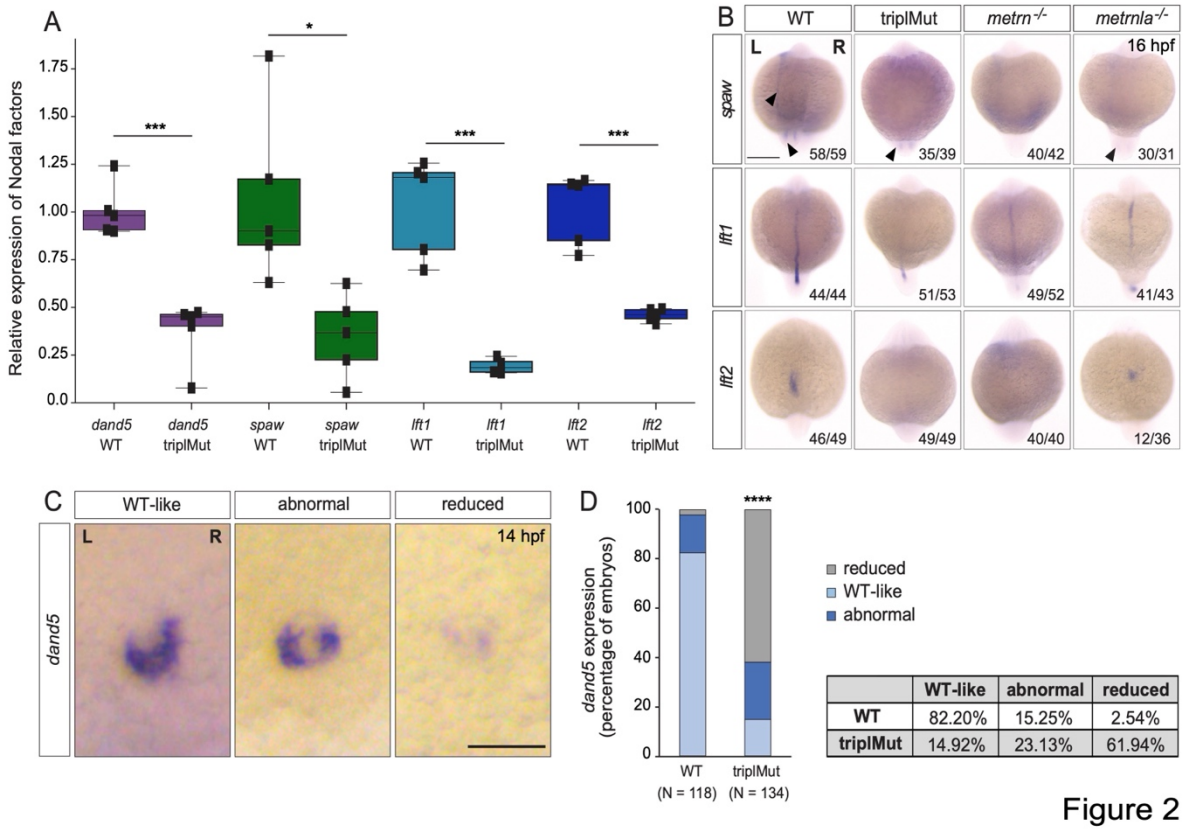

	WT-like	abnormal	reduced
WT	82.20%	15.25%	2.54%
triplMut	14.92%	23.13%	61.94%

719

Fig. 2. Metrns are required for proper Nodal factor genes expression. (**A**) qRT-PCR analysis for *dand5*, *spaw, lft1* and *lft2* expression in 14 hpf wild type (WT) and triplMut embryos (Student t-tests, ****p*-value: 0.00019 for *dand5;* **p*-value: 0.014 for *spaw*; ****p*-value: 0.0004 for *lft1*; ****p*-value: 0.00019 for *lft2*). (**B**) Dorsal view of 16 hpf triplMut, *metrn*$^{-/-}$ and *metrnla*$^{-/-}$ embryos with reduced expression of *spaw*, *lft1* and *lft2* as revealed by *in situ* hybridization. (**C**) *Dand5* expression at 14 hpf as revealed by *in situ* hybridization showing different transcripts distribution of *dand5* mRNA. (**D**) Quantification in percentage of *dand5* expression phenotypes at 14 hpf in WT and triplMut embryos, *****p*-value: <1.0e-5. Scale bar in (**B**): 250 µm, in (**C**): 100 µm; L= left, R=right.

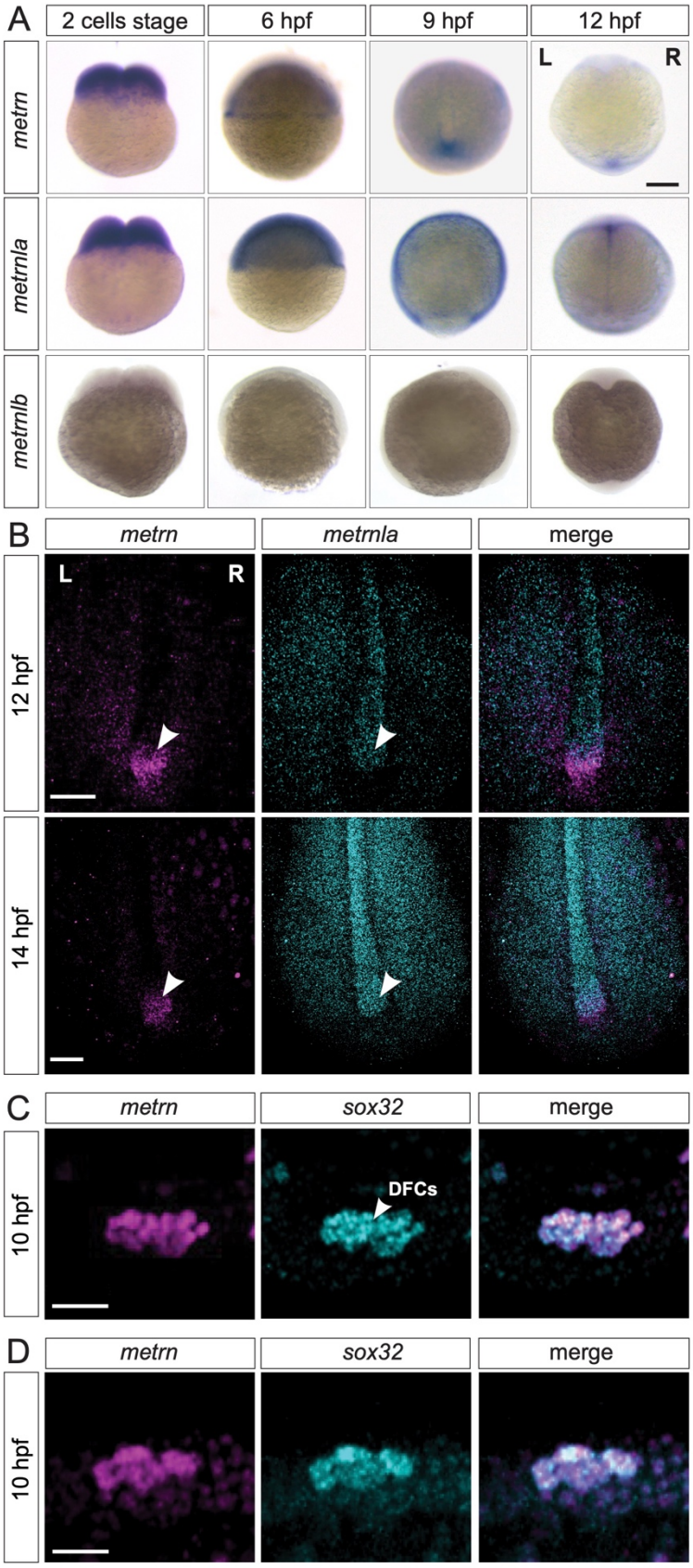

Figure 3

720

Fig. 3. *Metrns* are expressed during early zebrafish development. (**A**) Expression patterns of *metrn, metrnla* and *metrnlb* during early embryonic development from 2-cell stage to 12 hpf. (9hpf

and 12 hpf dorsal view) (**B**) Confocal cross-section of the midline region of 12 and 14 hpf zebrafish embryo showing mRNA expression of the *metrn* (magenta) and *metrnla* (cyan) and their co-expression in the area of the Kupffer's vesicle (KV, indicated by arrowheads) by HCR. (**C**) *Metrn* and *sox32* are co-expressed by dorsal forerunner cells (DFCs) as shown by double fluorescence *in situ* hybridization against *metrn* (magenta) and *sox32* (cyan) on 10 hpf wild type embryos. (**D**) *Metrnla* and *sox32* are co-expressed by DFCs as shown by double fluorescence *in situ* hybridization against *metrnla* (magenta) and *sox32* (cyan) on 10 hpf wild type embryos. Scale bars in (**A**): 500 µm, (**B**) 250 µm, (**C**) and (**D**): 50 µm. L = left, R = right.

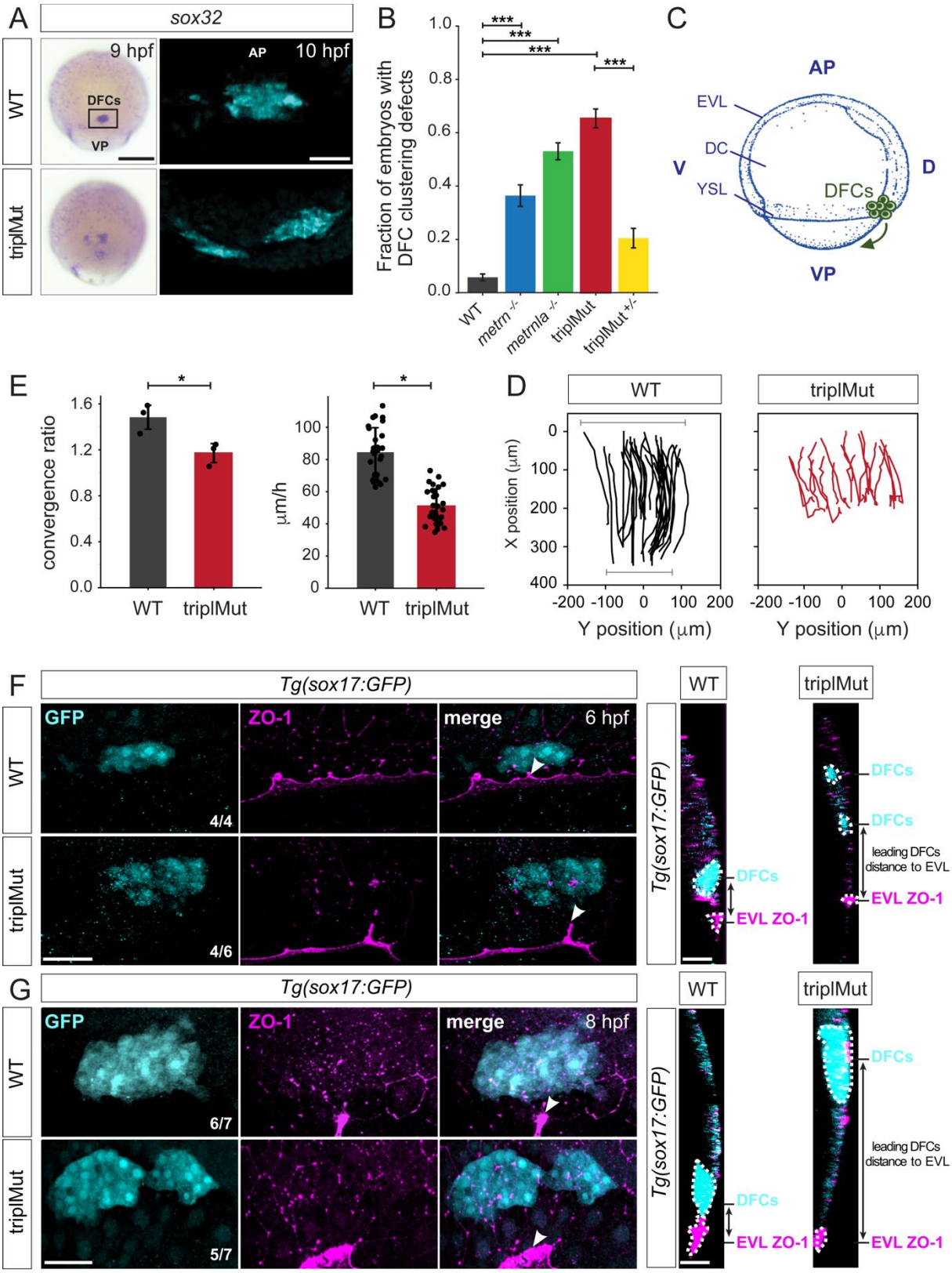
A
sox32
WT
triplMut
9 hpf
DFCs
VP
AP
10 hpf
B
Fraction of embryos with DFC clustering defects
1.0
0.8
0.6
0.4
0.2
0.0
***
***
***
***
WT
metrn -/-
metrnla -/-
triplMut
triplMut +/-
C
AP
EVL
DC
V
D
YSL
DFCs
VP
E
convergence ratio
1.6
1.2
0.8
0.4
0.0
*
WT
triplMut
μm/h
100
80
60
40
20
0
*
WT
triplMut
D
WT
triplMut
X position (μm)
0
100
200
300
400
-200 -100 0 100 200
Y position (μm)
-200 -100 0 100 200
Y position (μm)
F
Tg(sox17:GFP)
GFP
ZO-1
merge
6 hpf
WT
triplMut
4/4
4/6
Tg(sox17:GFP)
WT
triplMut
DFCs
DFCs
leading DFCs distance to EVL
DFCs
EVL ZO-1
EVL ZO-1
G
Tg(sox17:GFP)
GFP
ZO-1
merge
8 hpf
WT
triplMut
6/7
5/7
Tg(sox17:GFP)
WT
triplMut
DFCs
leading DFCs distance to EVL
DFCs
EVL ZO-1
EVL ZO-1

Figure 4

721

Fig. 4. *Metrns* loss-of-function leads to DFC clustering and migration defects. (**A**) Dorsal views of s*ox32* expression in DFCs at 9 hpf and 10 hpf (cyan) in wild type (WT) and triplMut embryos reveals DFC misclustering in triplMut embryos. (**B**) Quantification in fraction of embryos with DFC clustering defects at 9 hpf in WT, *metrn*$^{-/-}$, *metrnla*$^{-/-}$, triplMut and and triplMut$^{+/-}$ embryos (Fisher exact test, ****p*-value: 1.6e-07 for WT vs. *metrn*$^{-/-}$; ****p*-value: 3.5e-40 for WT vs. *metrnla*$^{-/-}$; ****p*-value: 1.5e-49 for WT vs. triplMut and ****p*-value: 7.9e-15 for triplMut vs. triplMut$^{+/-}$). (**C**) Lateral view of a schematic representation of an 8 hpf zebrafish embryo visualizing animal pole (AP) to vegetal pole (VP) dorsal forerunner cell (DFC) migration from both poles, adapted from [44]. (**D**) Tracking plots of combined DFC movement in wild type (left) and triplMut embryos (right) (n = 3 embryos per conditions, single embryo traces see Fig. S5D) showing directed DFC movement in both conditions. Bars indicating the analyzed stretch of tracked cells along the y-axis at the beginning and end of each recording. (**E**) Plots for convergence (upper) and migration speed (lower) analyzed from DFC tracking data show significant decrease in these parameters in triplMut embryos compared to WT controls. (**p*-value convergence ratio: 0.0295; ****p*-value for migration speed 1.217e-04) (**F-G**) GFP and ZO-1 immunostainings of the dorsal margin and confocal microscopy ZY-planes (right panels) of *Tg*(*sox17*:GFP) WT and triplMut embryos at (**F**) 6 hpf and (**G**) 8 hpf (shield stage and 75% epiboly) showing the apical domains of marginal DFCs with ZO-1 enriched junction points (arrowheads) and revealing the absence of apical ZO1-enrichment and detachment from the EVl/YSL in triplMut embryos. EVL, enveloping layer; DC, deep cells; YSL, yolk syncytial layer; D, dorsal; V, ventral. Scale bars in (**A**): 50 µm, (**F-G**): 50 µm. AP = animal pole, VP = vegetal pole.

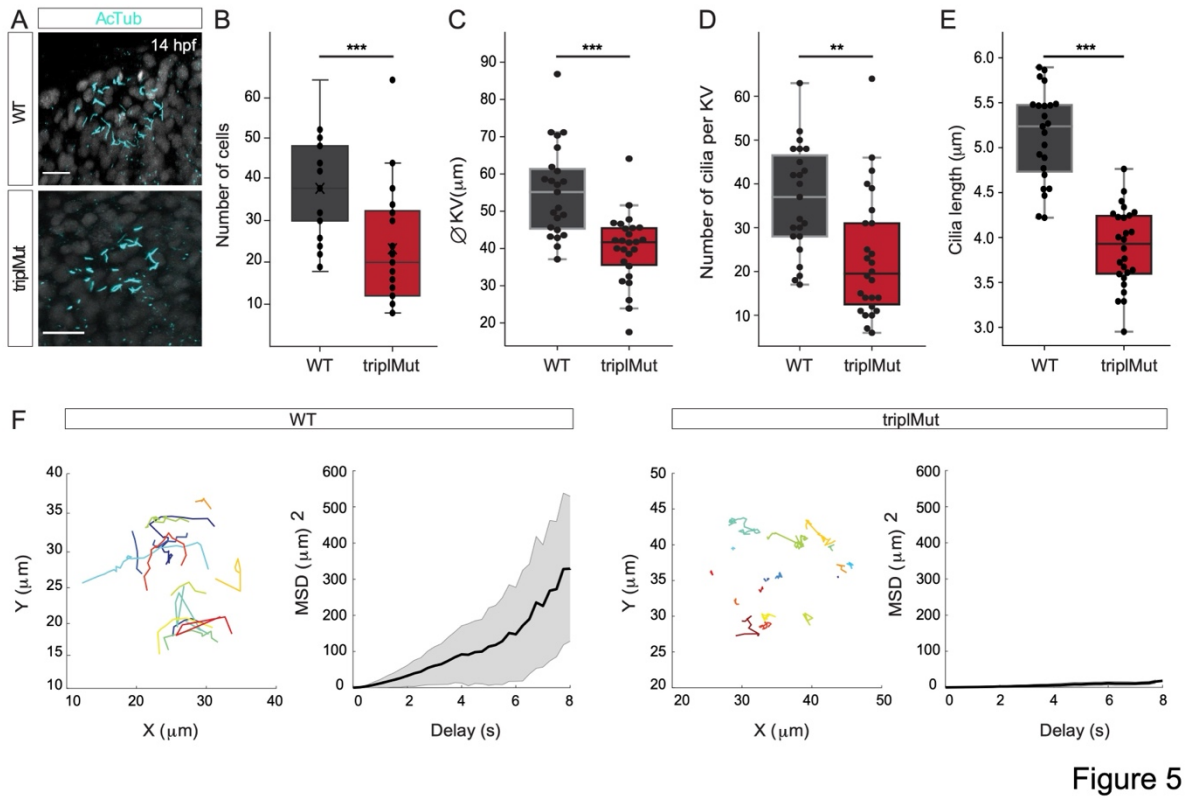

Figure 5

722

Fig. 5. *Metrns* loss-of-function impairs the Kupffer's vesicle formation and function. (**A**) Confocal cross-section of 14 hpf wild type (WT) and triplMut counterstained with acetylated tubulin (AcTub) labeling the cilia of the Kupffer's vesicle (KV). (**B**) The quantification of the cell number per KV in WT and triplMut embryos at 14 hpf shows a significant difference. (**C**) The KV diameter size measurement, (**D**) cilia number per KV quantification and (**E**) individual cilia length measurement in WT and triplMut embryos at 14 hpf are all significantly decreased in triplMut (N WT: 23, N triplMut: 26, Student t-tests, ****p*-value: 0.00028 for KV cell number, ****p*-value: 9.7e-06 for KV diameter size, ***p*-value: 0.0012 for cilia number. For cilia length: average per KV and ****p*-value: 5.8e-12). (**F**) Single microbeads tracking in the KV of 12 hpf -14 hpf WT and triplMut embryos and the mean square displacement (MSD), revealing a directed trajectory in WT samples in contrast to triplMut, displaying short and undirected trajectories**.** Scale bar in (**A**): 20 µm.

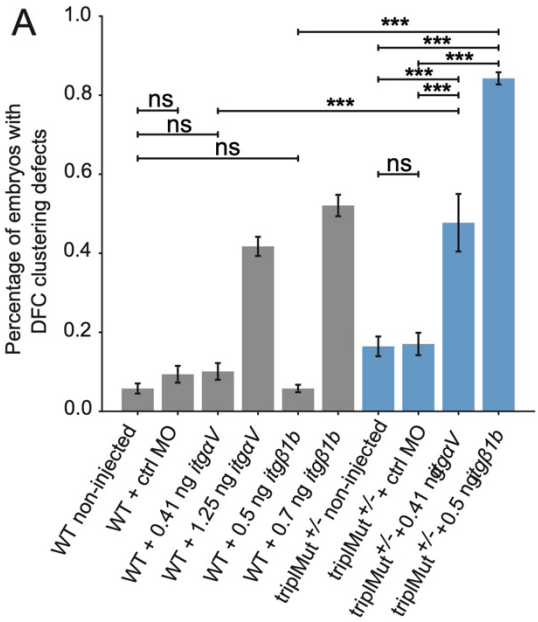

	WT-like	DFC clustering defects
WT non-injected	94.22%	5.78%
WT + ctrl MO	90.62%	9.38%
WT + 0.41 ng *itgαV*	89.90%	10.10%
WT + 1.25 ng *itgαV*	58.25%	41.75%
WT + 0.5 ng *itgβ1b*	94.22%	5.78%
WT + 0.7 ng *itgβ1b*	47.92%	52.08%
triplMut$^{+/-}$ non-injected	83.56%	16.44%
triplMut$^{+/-}$ + ctrl MO	82.95%	17.05%
triplMut$^{+/-}$+ 0.41 ng *itgαV*	35.16%	64.84%
triplMut$^{+/-}$+ 0.5 ng *itgβ1b*	15.74%	84.26%

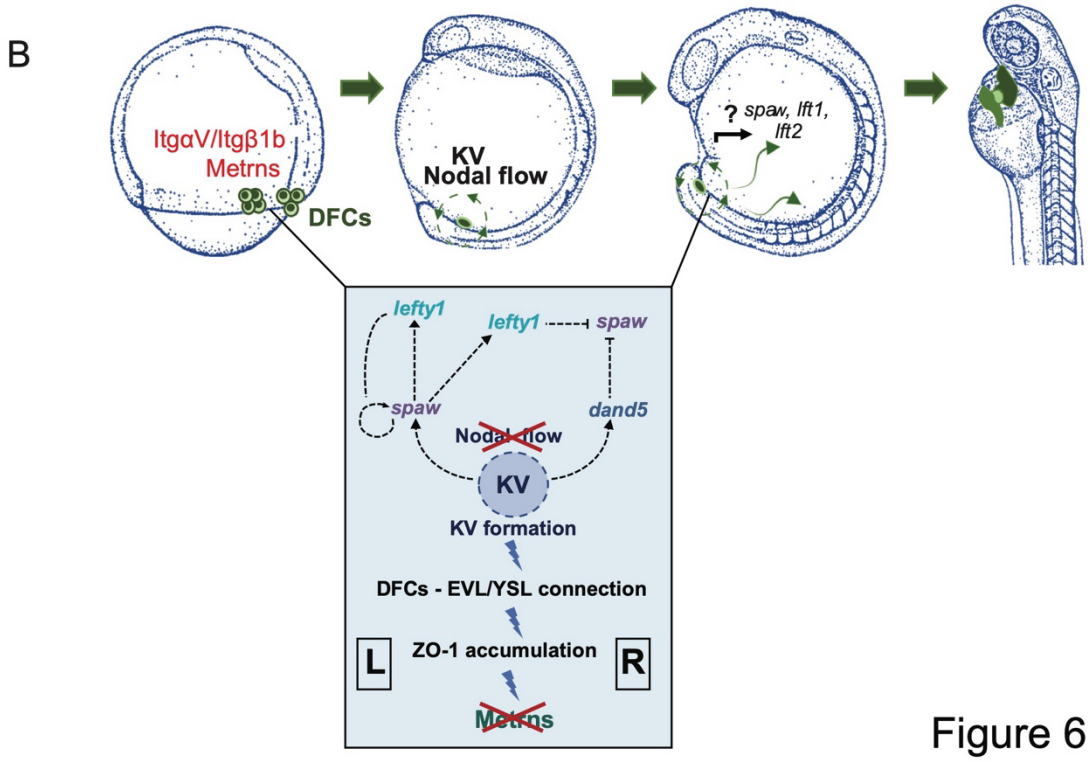

Figure 6

723

Fig. 6. Metrns and ItgαV/Itgβ1b act together for the proper clustering and migration of DFCs. (**A**) Quantification in percentage of embryos with DFC clustering defects at 9 hpf in non-injected wild type (WT), WT + 2.5 ng control morpholino (WT + ctrl MO), WT + insufficient doses of *itgαV/itgβ1b* MOs (WT + 0.41 ng *itgαV*; WT + 0.5 ng *itgβ1b*), WT + sufficient *itgαV/itgβ1b* MO doses (WT+ 1.25 ng *itgαV*; WT + 0.7 ng *itgβ1b*), triplMut$^{+/-}$ non-injected, triplMut$^{+/-}$ + 2.5ng ctrl MO and triplMut$^{+/-}$ with insufficient doses of *itgαV/itgβ1b* MOs (triplMut$^{+/-}$ + 0.41 ng *itgαV*; triplMut$^{+/-}$ + 0.5 ng *itgβ1b*). Fisher

exact tests indicate *p-value < 0.01, **p-value < 0.001 and ***p-value < 0.0001 and ns = not significant. (**B**) Schematic representation modeling the novel role of Metrns for DFCs assembly and migration, for the proper KV formation and subsequent Nodal factors expression distribution at the base of the correct L-R axis establishment during early development (adapted from [44]).

724

REFERENCES

[1] Blum, M., Feistel, K., Thumberger, T., and Schweickert, A. (2014) The evolution and conservation of left-right patterning mechanisms. *Development*. 141 (8), 1603–1613.

[2] Blum, M. and Ott, T. (2018) Animal left–right asymmetry. *Current Biology*. 28 (7), R301–R304.

[3] Grimes, D.T. and Burdine, R.D. (2017) Left–Right Patterning: Breaking Symmetry to Asymmetric Morphogenesis. *Trends in Genetics*. 33 (9), 616–628.

[4] Kawasumi, A., Nakamura, T., Iwai, N., Yashiro, K., Saijoh, Y., Belo, J.A., et al. (2011) Left–right asymmetry in the level of active Nodal protein produced in the node is translated into left–right asymmetry in the lateral plate of mouse embryos. *Developmental Biology*. 353 (2), 321–330.

[5] Branford, W.W. and Yost, H.J. (2004) Nodal Signaling: CrypticLefty Mechanism of Antagonism Decoded. *Current Biology*. 14 (9), R341–R343.

[6] Zhou, X., Lowe, L., Sasaki, H., Hogan, B.L.M., and Kuehn, M.R. (1993) Nodal is a novel TGF-β-like gene expressed in the mouse node during gastrulation. *Nature*. 361 (6412), 543–547.

[7] Chen, Y. and Schier, A.F. (2002) Lefty Proteins Are Long-Range Inhibitors of Squint-Mediated Nodal Signaling. *Current Biology*. 12 (24), 2124–2128.

[8] Chen, C. and Shen, M.M. (2004) Two Modes by which Lefty Proteins Inhibit Nodal Signaling. *Current Biology*. 14 (7), 618–624.

[9] Essner, J.J., Amack, J.D., Nyholm, M.K., Harris, E.B., and Yost, H.J. (2005) Kupffer's vesicle is a ciliated organ of asymmetry in the zebrafish embryo that initiates left-right development of the brain, heart and gut. *Development*. 132 (6), 1247–1260.

[10] Vick, P., Schweickert, A., Weber, T., Eberhardt, M., Mencl, S., Shcherbakov, D., et al. (2009) Flow on the right side of the gastrocoel roof plate is dispensable for symmetry breakage in the frog Xenopus laevis. *Developmental Biology*. 331 (2), 281–291.

[11] Nonaka, S., Shiratori, H., Saijoh, Y., and Hamada, H. (2002) Determination of left–right patterning of the mouse embryo by artificial nodal flow. *Nature*. 418 (6893), 96–99.

[12] Schweickert, A., Weber, T., Beyer, T., Vick, P., Bogusch, S., Feistel, K., et al. (2007) Cilia-Driven Leftward Flow Determines Laterality in Xenopus. *Current Biology*. 17 (1), 60–66.

[13] Okada, Y., Takeda, S., Tanaka, Y., Belmonte, J.-C.I., and Hirokawa, N. (2005) Mechanism of Nodal Flow: A Conserved Symmetry Breaking Event in Left-Right Axis Determination. *Cell*. 121 (4), 633–644.

[14] Tanaka, Y., Okada, Y., and Hirokawa, N. (2005) FGF-induced vesicular release of Sonic hedgehog and retinoic acid in leftward nodal flow is critical for left–right determination. *Nature*. 435 (7039), 172–177.

[15] Nonaka, S., Tanaka, Y., Okada, Y., Takeda, S., Harada, A., Kanai, Y., et al. (1998) Randomization of Left–Right Asymmetry due to Loss of Nodal Cilia Generating Leftward Flow of Extraembryonic Fluid in Mice Lacking KIF3B Motor Protein. *Cell*. 95 (6), 829–837.

[16] Smith, D.J., Montenegro-Johnson, T.D., and Lopes, S.S. (2019) Symmetry-Breaking Cilia-Driven Flow in Embryogenesis. *Annual Review of Fluid Mechanics*. 51 (1), 105–128.

[17] Schoenwolf, G.C., Bleyl, S.B., Brauer, P.R., and Francis-West, P.H. (2014) Larsen's Human Embryology. Elsevier Health Sciences, .

775 [18] Hamada, H., Meno, C., Watanabe, D., and Saijoh, Y. (2002) Establishment of
776 vertebrate left–right asymmetry. *Nature Reviews Genetics*. 3 (2), 103–113.
777 [19] Gros, J., Feistel, K., Viebahn, C., Blum, M., and Tabin, C.J. (2009) Cell
778 Movements at Hensen's Node Establish Left/Right Asymmetric Gene
779 Expression in the Chick. *Science*. 324 (5929), 941–944.
780 [20] Essner, J.J., Vogan, K.J., Wagner, M.K., Tabin, C.J., Yost, H.J., and
781 Brueckner, M. (2002) Conserved function for embryonic nodal cilia. *Nature*. 418
782 (6893), 37–38.
783 [21] Stephen, L.A., Johnson, E.J., Davis, G.M., McTeir, L., Pinkham, J., Jaberi, N.,
784 et al. (2014) The chicken left right organizer has nonmotile cilia which are lost
785 in a stage-dependent manner in the talpid3 ciliopathy. *Genesis (New York,*
786 *N.y. : 2000)*. 52 (6), 600–613.
787 [22] Oteíza, P., Köppen, M., Concha, M.L., and Heisenberg, C.-P. (2008) Origin
788 and shaping of the laterality organ in zebrafish. *Development*. 135 (16), 2807–
789 2813.
790 [23] Cooper, M.S. and D'amico, L.A. (1996) A Cluster of Noninvoluting Endocytic
791 Cells at the Margin of the Zebrafish Blastoderm Marks the Site of Embryonic
792 Shield Formation. *Developmental Biology*. 180 (1), 184–198.
793 [24] Pulgar, E., Schwayer, C., Guerrero, N., López, L., Márquez, S., Härtel, S., et
794 al. (2021) Apical contacts stemming from incomplete delamination guide
795 progenitor cell allocation through a dragging mechanism. *eLife*. 10 e66483.
796 [25] Kramer-Zucker, A.G., Olale, F., Haycraft, C.J., Yoder, B.K., Schier, A.F., and
797 Drummond, I.A. (2005) Cilia-driven fluid flow in the zebrafish pronephros, brain
798 and Kupffer's vesicle is required for normal organogenesis. *Development*. 132
799 (8), 1907–1921.
800 [26] Hirokawa, N., Tanaka, Y., Okada, Y., and Takeda, S. (2006) Nodal Flow and
801 the Generation of Left-Right Asymmetry. *Cell*. 125 (1), 33–45.
802 [27] Harvey, R.P. (1998) Links in the Left/Right Axial Pathway. *Cell*. 94 (3), 273–
803 276.
804 [28] Kim, Y.-Y., Moon, J.-S., Kwon, M., Shin, J., Im, S.-K., Kim, H.-A., et al. (2014)
805 Meteorin Regulates Mesendoderm Development by Enhancing Nodal
806 Expression. *PLoS ONE*. 9 (2), e88811.
807 [29] Nishino, J., Yamashita, K., Hashiguchi, H., Fujii, H., Shimazaki, T., and
808 Hamada, H. (2004) Meteorin: a secreted protein that regulates glial cell
809 differentiation and promotes axonal extension. *The EMBO Journal*. 23 (9),
810 1998–2008.
811 [30] Ramialison, M., Bajoghli, B., Aghaallaei, N., Ettwiller, L., Gaudan, S., Wittbrodt,
812 B., et al. (2008) Rapid identification of PAX2/5/8 direct downstream targets in
813 the otic vesicle by combinatorial use of bioinformatics tools. *Genome Biology*. 9
814 (10), R145.
815 [31] Jørgensen, J.R., Fransson, A., Fjord-Larsen, L., Thompson, L.H., Houchins,
816 J.P., Andrade, N., et al. (2012) Cometin is a novel neurotrophic factor that
817 promotes neurite outgrowth and neuroblast migration in vitro and supports
818 survival of spiral ganglion neurons in vivo. *Experimental Neurology*. 233 (1),
819 172–181.
820 [32] El-Brolosy, M.A., Kontarakis, Z., Rossi, A., Kuenne, C., Günther, S., Fukuda,
821 N., et al. (2019) Genetic compensation triggered by mutant mRNA degradation.
822 *Nature*. 568 (7751), 193–197.

[33] Montague, T.G., Gagnon, J.A., and Schier, A.F. (2018) Conserved regulation of Nodal-mediated left-right patterning in zebrafish and mouse. *Development*. 145 (24), dev171090.
[34] Long, S., Ahmad, N., and Rebagliati, M. (2003) The zebrafish *nodal* -related gene *southpaw* is required for visceral and diencephalic left-right asymmetry. *Development*. 130 (11), 2303–2316.
[35] Brennan, J., Norris, D.P., and Robertson, E.J. (2002) Nodal activity in the node governs left-right asymmetry. *Genes & Development*. 16 (18), 2339–2344.
[36] Saijoh, Y., Oki, S., Ohishi, S., and Hamada, H. (2003) Left–right patterning of the mouse lateral plate requires Nodal produced in the node. *Developmental Biology*. 13.
[37] Pelliccia, J.L., Jindal, G.A., and Burdine, R.D. (2017) Gdf3 is required for robust Nodal signaling during germ layer formation and left-right patterning. *eLife*. 6 e28635.
[38] Hojo, M., Takashima, S., Kobayashi, D., Sumeragi, A., Shimada, A., Tsukahara, T., et al. (2007) Right-elevated expression of charon is regulated by fluid flow in medaka Kupffer's vesicle: Left-right asymmetric expression of charon. *Development, Growth & Differentiation*. 49 (5), 395–405.
[39] Gourronc, F., Ahmad, N., Nedza, N., Eggleston, T., and Rebagliati, M. (2007) Nodal activity around Kupffer's vesicle depends on the T-box transcription factors notail and spadetail and on notch signaling. *Developmental Dynamics*. 236 (8), 2131–2146.
[40] Alexander, J., Rothenberg, M., Henry, G.L., and Stainier, D.Y.R. (1999) casanova Plays an Early and Essential Role in Endoderm Formation in Zebrafish. *Developmental Biology*. 215 (2), 343–357.
[41] Kikuchi, Y., Agathon, A., Alexander, J., Thisse, C., Waldron, S., Yelon, D., et al. (2001) *casanova* encodes a novel Sox-related protein necessary and sufficient for early endoderm formation in zebrafish. *Genes & Development*. 15 (12), 1493–1505.
[42] Amack, J.D. and Yost, H.J. (2004) The T Box Transcription Factor No Tail in Ciliated Cells Controls Zebrafish Left-Right Asymmetry. *Current Biology*. 14 (8), 685–690.
[43] Matsui, T., Hiroshi, I., and Yasumasa, B. (2015) Cell collectivity regulation within migrating cell cluster during Kupffer's vesicle formation in zebrafish. *Frontiers in Cell and Developmental Biology*. 3 8.
[44] Kimmel, C.B., Ballard, W.W., Kimmel, S.R., Ullmann, B., and Schilling, T.F. (1995) Stages of embryonic development of the zebrafish. *Developmental Dynamics*. 203 (3), 253–310.
[45] Hashimoto, H., Rebagliati, M., Ahmad, N., Muraoka, O., Kurokawa, T., Hibi, M., et al. (2004) The Cerberus/Dan-family protein Charon is a negative regulator of Nodal signaling during left-right patterning in zebrafish. *Development*. 131 (8), 1741–1753.
[46] Sampaio, P., Ferreira, R.R., Guerrero, A., Pintado, P., Tavares, B., Amaro, J., et al. (2014) Left-Right Organizer Flow Dynamics: How Much Cilia Activity Reliably Yields Laterality? *Developmental Cell*. 29 (6), 716–728.
[47] Gokey, J.J., Ji, Y., Tay, H.G., Litts, B., and Amack, J.D. (2016) Kupffer's vesicle size threshold for robust left-right patterning of the zebrafish embryo: Size Threshold For KV Function. *Developmental Dynamics*. 245 (1), 22–33.

871 [48] de Bruin, K., Ruthardt, N., von Gersdorff, K., Bausinger, R., Wagner, E., Ogris,
872 M., et al. (2007) Cellular Dynamics of EGF Receptor–Targeted Synthetic
873 Viruses. *Molecular Therapy*. 15 (7), 1297–1305.
874 [49] Hynes, R.O. (1992) Integrins: Versatility, modulation, and signaling in cell
875 adhesion. *Cell*. 69 (1), 11–25.
876 [50] Ablooglu, A.J., Tkachenko, E., Kang, J., and Shattil, S.J. (2010) Integrin αV is
877 necessary for gastrulation movements that regulate vertebrate body
878 asymmetry. *Development*. 137 (20), 3449–3458.
879 [51] Reboll, M.R., Klede, S., Taft, M.H., Cai, C.-L., Field, L.J., Lavine, K.J., et al.
880 (2022) Meteorin-like promotes heart repair through endothelial KIT receptor
881 tyrosine kinase. *Science*. 376 (6599), 1343–1347.
882 [52] Ushach, I., Arrevillaga-Boni, G., Heller, G.N., Pone, E., Hernandez-Ruiz, M.,
883 Catalan-Dibene, J., et al. (2018) Meteorin-like/Meteorin-β Is a Novel
884 Immunoregulatory Cytokine Associated with Inflammation. *The Journal of*
885 *Immunology*. 201 (12), 3669–3676.
886 [53] Kim, Y.J., VijayKumar, S., Iovino, B., Granados, A., Ancheta, S., Zhao, X., et
887 al. (2024) Zebrahub-Multiome: Uncovering Gene Regulatory Network
888 Dynamics During Zebrafish Embryogenesis.
889 [54] Bisgrove, B.W., Essner, J.J., and Yost, H.J. (2000) Multiple pathways in the
890 midline regulate concordant brain, heart and gut left-right asymmetry.
891 *Development*. 127 (16), 3567–3579.
892 [55] Solnica-Krezel, L., Stemple, D.L., Mountcastle-Shah, E., Rangini, Z.,
893 Neuhauss, S.C., Malicki, J., et al. (1996) Mutations affecting cell fates and
894 cellular rearrangements during gastrulation in zebrafish. *Development*. 123 (1),
895 67–80.
896 [56] Oteiza, P., Köppen, M., Krieg, M., Pulgar, E., Farias, C., Melo, C., et al. (2010)
897 Planar cell polarity signalling regulates cell adhesion properties in progenitors
898 of the zebrafish laterality organ. *Development*. 137 (20), 3459–3468.
899 [57] Choi, W.-Y., Giraldez, A.J., and Schier, A.F. (2007) Target Protectors Reveal
900 Dampening and Balancing of Nodal Agonist and Antagonist by miR-430.
901 *Science*. 318 (5848), 271–274.
902 [58] Milner, R., Edwards, G., Streuli, C., and ffrench-Constant, C. (1996) A Role in
903 Migration for the αvβ1 Integrin Expressed on Oligodendrocyte Precursors. *The*
904 *Journal of Neuroscience*. 16 (22), 7240–7252.
905 [59] Felding-Habermann, B., Silletti, S., Mei, F., Siu, C.-H., Yip, P.M., Brooks, P.C.,
906 et al. (1997) A Single Immunoglobulin-like Domain of the Human Neural Cell
907 Adhesion Molecule L1 Supports Adhesion by Multiple Vascular and Platelet
908 Integrins. *Journal of Cell Biology*. 139 (6), 1567–1581.
909 [60] Jülich, D., Mould, A.P., Koper, E., and Holley, S.A. (2009) Control of
910 extracellular matrix assembly along tissue boundaries via Integrin and
911 Eph/Ephrin signaling. *Development*. 136 (17), 2913–2921.
912 [61] Dai, Y.-W., Ma, J.-K., Jiang, R., Zhan, X.-L., Chen, S.-Y., Feng, L.-L., et al.
913 (2022) Meteorin links the bone marrow hypoxic state to hematopoietic
914 stem/progenitor cell mobilization. *Cell Reports*. 40 (12), 111361.
915 [62] Mellgren, E.M. and Johnson, S.L. (2005) kitb, a second zebrafish ortholog of
916 mouse Kit. *Development Genes and Evolution*. 215 (9), 470–477.
917 [63] Zheng, S., Li, Z., Song, J., Liu, J., and Miao, C. (2016) Metrnl: a secreted
918 protein with new emerging functions. *Acta Pharmacologica Sinica*. 37 (5), 571–
919 579.

[64] Hwang, W.Y., Fu, Y., Reyon, D., Maeder, M.L., Tsai, S.Q., Sander, J.D., et al. (2013) Efficient genome editing in zebrafish using a CRISPR-Cas system. *Nature Biotechnology*. 31 (3), 227–229.
[65] Thisse, C. and Thisse, B. (2008) High-resolution in situ hybridization to whole-mount zebrafish embryos. *Nature Protocols*. 3 (1), 59–69.
[66] Streit, A. and Stern, C.D. (2001) Combined Whole-Mount in Situ Hybridization and Immunohistochemistry in Avian Embryos. *Methods*. 23 (4), 339–344.
[67] Pulgar, E., Schwayer, C., Guerrero, N., López, L., Márquez, S., Härtel, S., et al. (2021) Apical contacts stemming from incomplete delamination guide progenitor cell allocation through a dragging mechanism. *eLife*. 10 e66483.
[68] Tang, R., Dodd, A., Lai, D., McNabb, W.C., and Love, D.R. (2007) Validation of Zebrafish (Danio rerio) Reference Genes for Quantitative Real-time RT-PCR Normalization. *Acta Biochimica et Biophysica Sinica*. 39 (5), 384–390.
[69] Valcu, M. and Valcu, C.-M. (2011) Data transformation practices in biomedical sciences. *Nature Methods*. 8 (2), 104–105.
[70] Borovina, A., Superina, S., Voskas, D., and Ciruna, B. (2010) Vangl2 directs the posterior tilting and asymmetric localization of motile primary cilia. *Nature Cell Biology*. 12 (4), 407–412.
[71] Sbalzarini, I.F. and Koumoutsakos, P. (2005) Feature point tracking and trajectory analysis for video imaging in cell biology. *Journal of Structural Biology*. 151 (2), 182–195.
[72] Tarantino, N., Tinevez, J.-Y., Crowell, E.F., Boisson, B., Henriques, R., Mhlanga, M., et al. (2014) TNF and IL-1 exhibit distinct ubiquitin requirements for inducing NEMO–IKK supramolecular structures. *Journal of Cell Biology*. 204 (2), 231–245.
[73] Zwillinger, D. (2022) CRC Standard Mathematical Tables and Formulae, 31st Edition (Advances in Applied Mathematics) 31st Edition. 31st ed. Chapman and Hall/CRC, .
[74] Papoulis, A. (1984) Probability, random variables, and stochastic processes. McGraw-Hill Inc.,US, .
[75] Dereeper, A., Guignon, V., Blanc, G., Audic, S., Buffet, S., Chevenet, F., et al. (2008) Phylogeny.fr: robust phylogenetic analysis for the non-specialist. *Nucleic Acids Research*. 36 (Web Server issue), W465–W469.
[76] Dereeper, A., Audic, S., Claverie, J.-M., and Blanc, G. (2010) BLAST-EXPLORER helps you building datasets for phylogenetic analysis. *BMC Evolutionary Biology*. 10 8.
[77] Edgar, R.C. (2004) MUSCLE: multiple sequence alignment with high accuracy and high throughput. *Nucleic Acids Research*. 32 (5), 1792–1797.
[78] Castresana, J. (2000) Selection of Conserved Blocks from Multiple Alignments for Their Use in Phylogenetic Analysis. *Molecular Biology and Evolution*. 17 (4), 540–552.
[79] Guindon, S. and Gascuel, O. (2003) A Simple, Fast, and Accurate Algorithm to Estimate Large Phylogenies by Maximum Likelihood. *Systematic Biology*. 52 (5), 696–704.
[80] Anisimova, M. and Gascuel, O. (2006) Approximate Likelihood-Ratio Test for Branches: A Fast, Accurate, and Powerful Alternative. *Systematic Biology*. 55 (4), 539–552.
[81] Chevenet, F., Brun, C., Bañuls, A.-L., Jacq, B., and Christen, R. (2006) TreeDyn: towards dynamic graphics and annotations for analyses of trees. *BMC Bioinformatics*. 7 439.

RESOURCE AVAILABILITY

Lead contact

Requests for further information and resources should be directed to and will be fulfilled by the lead contact, Filippo Del Bene (filippo.del-bene@inserm.fr).

Materials availability

All unique/stable reagents generated in this study are available from the lead contact with a completed materials transfer agreement.

Data and Code Availability

•All data reported in the paper are available from the lead contact upon request.

•This paper does report original code which is available at https://github.com/jboulanger91/meteorin. Codes for statistical analysis are available at https://github.com/FannyEggeler/Meteorin_analysis.

•Any additional information required to reanalyze the data reported in this paper is available from the lead contact upon request.

ACKNOWLEDGEMENTS

We thank all members of the Del Bene lab for discussions, the Institut Curie and Institut de la Vision imaging and animal facilities. We acknowledge the lab of Jean Livet for their support with the chick analysis. We would like to thank Pierre Luc Bardet from IBPS (Sorbonne Université) for fruitful discussions. We thank Clémence Gentner from Gilles Tessier's lab at the Institut de la Vision for the microspheres sample. We thank Marco Molari (Biozentrum Basel) for the support with the statistical analysis. Work in the Del Bene laboratory was supported by ANR MetAxon [ANR-17-CE16-0007], the IHU FOReSIGHT [ANR-18-IAHU-0001], CNRS, INSERM, and Sorbonne Université core funding. F.E. was supported by the École des Neurosciences de Paris (ENP) Ile-de-France network and the Fondation pour la Recherche Médicale (FRM). F.D.S. was supported by a doctoral fellowship of the Curie International PhD program. T.O.A. was supported by a Boehringer Ingelheim Fonds PhD Fellowship.

AUTHORS CONTRIBUTION

F.E. did the experimental work and analyzed the results. L.B. contributed to the experimental work. F.D.S., T.A and K.D. generated the CRISPR/Cas9 *metrn* mutant lines. J.B.W performed the KV microbeads tracking analysis and analyzed the cell's tracking experiment. F.E, S.A.

and F.D.B. conceived the project and wrote the manuscript. S.A. and F.D.B. co-supervised the study. All the authors reviewed and edited the manuscript.

DECLARATION OF INTERESTS

The authors declare no competing interests.

1011 **SUPPLEMENTARY FIGURES**

1012

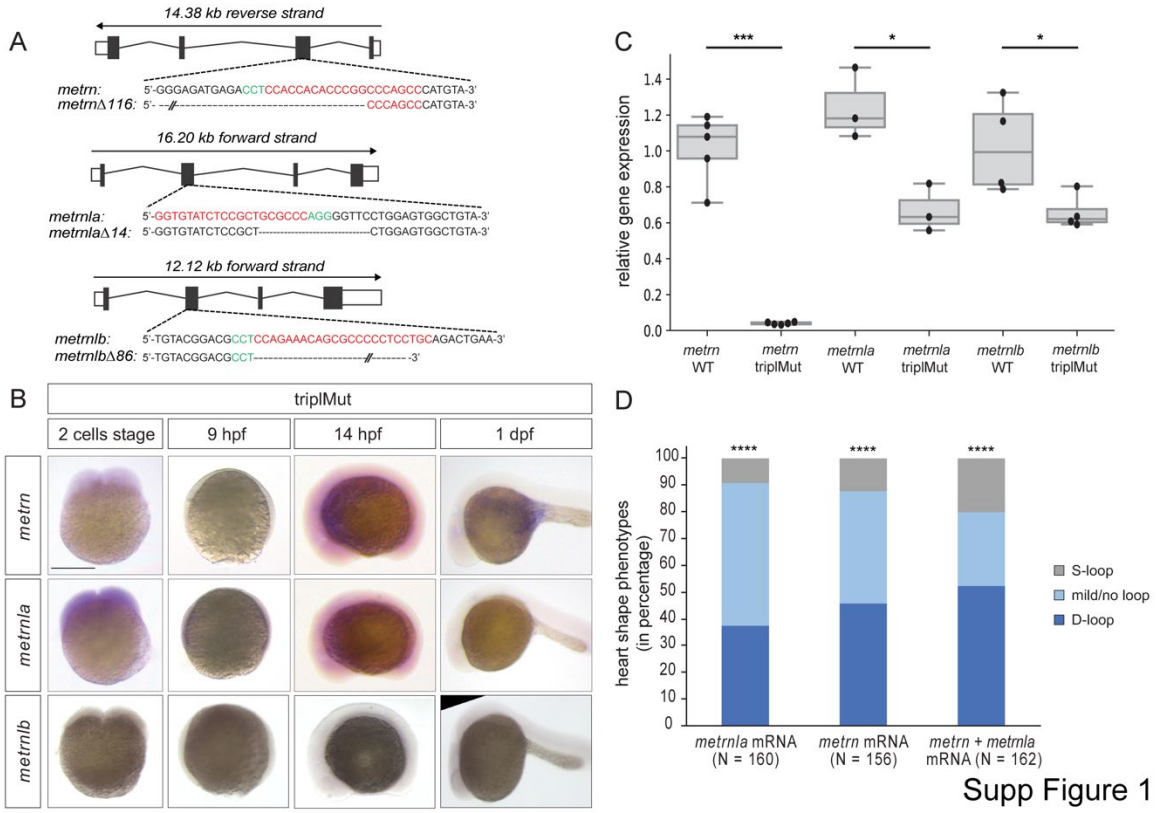

Fig. S1. (A-C) *Metrn* genes CRISPR/Cas9 mediated knockout generation and validation. (D) *Metrns* loss of function effect on heart morphology. (**A**) Targeted *metrns* loci in the zebrafish genome for knockout generation. Red highlights the sgRNA homologous sequence and PAM sequences are highlighted in green. The generated mutation is indicated below by dashed lines and the number of deleted nucleotides is indicated after the Δ sign. (**B**) *Metrn, metrnla* and *metrnlb* expression in triplMut embryos from 2-cell stage to 1 day post fertilization (dpf) is highly reduced or undetectable by *in situ* hybridization (lateral views). (**C**) *Metrns* expression levels are reduced in triplMut embryos as shown by qRT-PCR analysis of *metrn*, *metrnla*, *metrnlb* expression level at 14 hpf for *metrn* and *metrnla* and at 48 hpf for *metrnlb* in wild type (WT) and triplMut embryos. (Student t-test, ****p*-value: 3.1e-06 for *metrn*; **p*-value: 0.014 for *metrnla*; **p*-value: 0.04 for *metrnlb*). (**D**) Quantification in percentage of the number of embryos with S-looped, D-looped or mild/no looped heart phenotypes at 2 dpf upon injection of *metrnla* mRNA, *metrn* mRNA or both in triplMut embryos. Displayed *p*-values compared to WT: ****p*-value: <1.0e-5 for *metrnla* mRNA, ****p*-value: <1.0e-5 for *metrn* mRNA, ****p*-value: <1.0e-5 for *metrn* + *metrnla* mRNA. Scale bar in (**B**) 250 µm.

1013

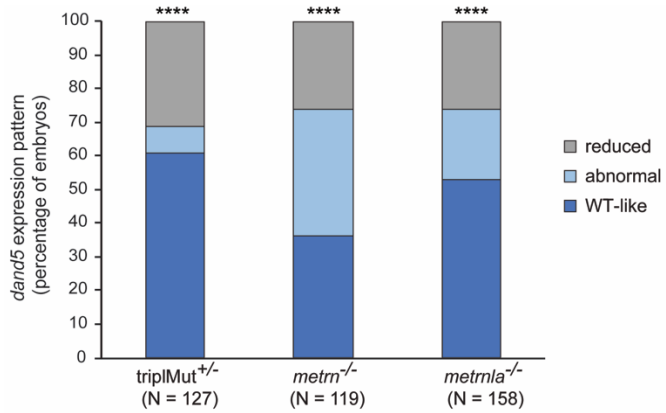

	WT-like	abnormal	reduced
triplMut$^{+/-}$	60.63%	7.87%	31.50%
metrn$^{-/-}$	39.50%	40.33%	28.57%
metrnla$^{-/-}$	53.16%	20.89%	25.95%

Supp Figure 2

Fig. S2. Nodal factors gene expression is altered in the absence of Metrns. Quantification of the number of embryos in percentage with reduced, inverted or wild type (WT) -like *dand5* expression pattern in 14 hpf triplMut$^{+/-}$, *metrn*$^{-/-}$ and *metrnla*$^{-/-}$ embryos, compared to WT, Permutation test, ****p-value <1.0e-5 for triplMut$^{+/-}$, ****p-value <1.0e-5 for *metrn*$^{-/-}$, ****p-value <1.0e-5 for *metrnla*$^{-/-}$.

1014

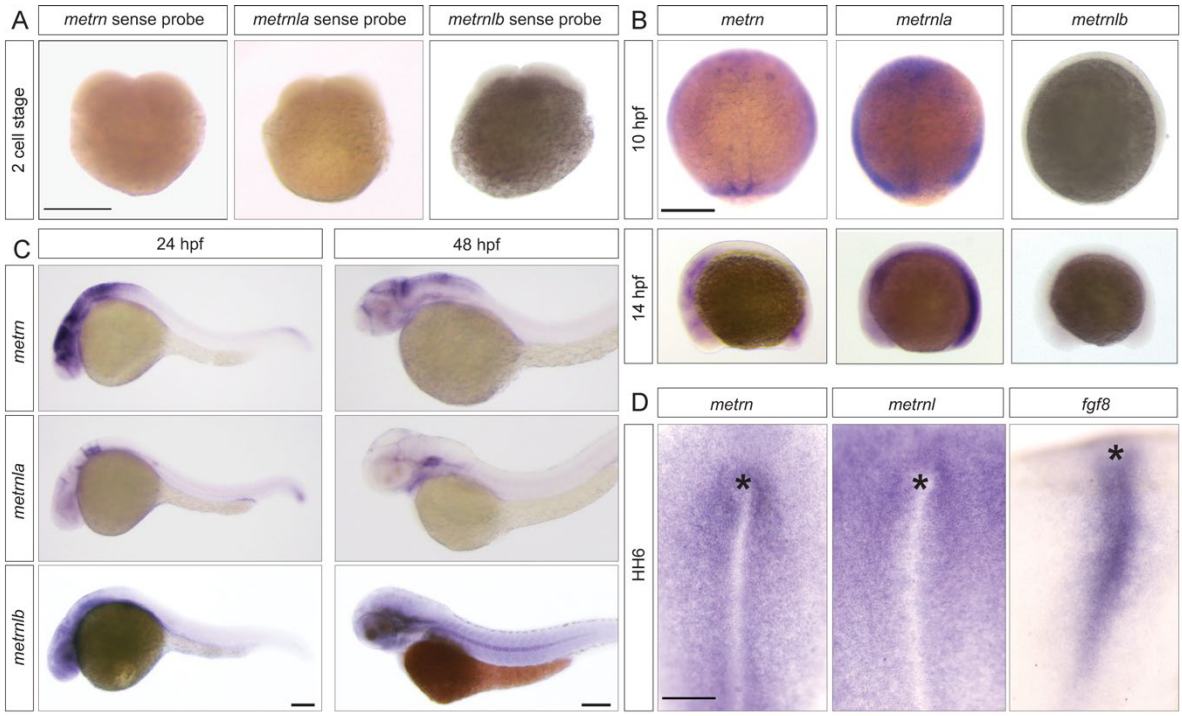

Supp Figure 3

Fig. S3. *Metrns* expression during early zebrafish and chick development. (**A**) No expression can be detected for *metrn, metrnla* and *metrnlb* upon *in situ* hybridization using sense *metrn, metrnla*

and *metrnlb* riboprobes on 2-cell stage wild type embryos. (**B**) *Metrn* expression at 10 hpf can be found in the leading edge of the shield and in the forming Kupffer's vesicle as shown by *in situ* hybridization (dorsal view) and at 14 hpf *metrn* transcripts can be detected in the area of the KV and the developing brain (later view). While *metrnla* at 10 hpf is expressed in the whole enveloping layer and developing midline as revealed here by *in situ* hybridization (dorsal view). At 14 hpf *metrnla* transcripts can be found in the area of the forming KV and midline (later view). No expression can be detected for *metrnlb* at these stages. (**C**) From 24 hpf, all *metrn* genes are expressed in the developing central nervous system as shown by *in situ* hybridization (lateral views). (**D**) Dorsal view of *metrn*, *metrnl* and *fgf8 in situ* hybridization in HH6 chick embryos reveal that *metrn*, *metrnl* are expressed around the Hensen's node (*) and the primitive streak during chick early embryonic development. Scale bars: in (**A, B** and **D**) 250 µm and in (**C**) 100 µm.

1015

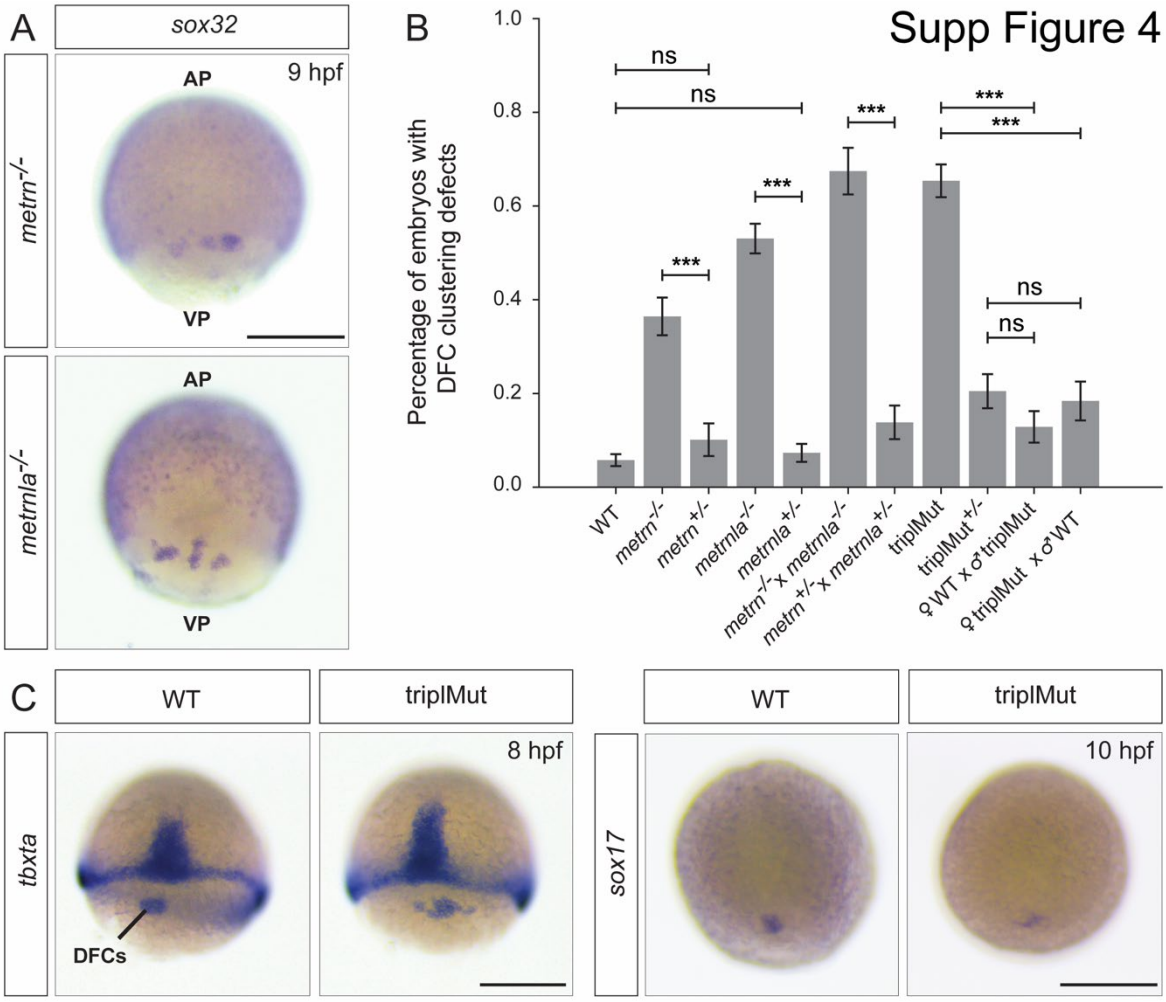

Fig. S4. *Metrns* loss-of-function leads to DFC disorganization and migration defects. (**A**) *Sox32* antisense riboprobe *in situ* hybridization revealing DFC misclustering in 9 hpf *metrn*$^{-/-}$ and *metrnla*$^{-/-}$ embryos. (**B**) Quantification in percentage of the number of embryos with DFC clustering defects at 9 hpf in wild type (WT) and several *metrns* mutant backgrounds (Fisher exact test, ***p-value: 1.5e-

05 for *metrn*$^{-/-}$ vs. *metrn*$^{+/-}$; ***p*-value: 2.5e-26 for *metrnla*$^{-/-}$ vs. *metrnla*$^{+/-}$; ***p*-value: 1.2e-13 for *metrn*$^{-/-}$ x *metrnla*$^{-/-}$ vs. *metrn*$^{+/-}$ x *metrnla*$^{+/-}$; ***p*-value: 2.2e-18 for triplMut vs. ♀WT x ♂triplMut and ***p*-value: 2.1e-13 for triplMut vs. ♀triplMut x ♂WT) (**C**) *tbxta* and *sox17* DFC specification markers are expressed in the absence of Metrn proteins as shown by *in situ* hybridization on WT and triplMut at 8 and 10 dpf respectively. Scale bars: in **A** and **C** 0.5 mm.

1016

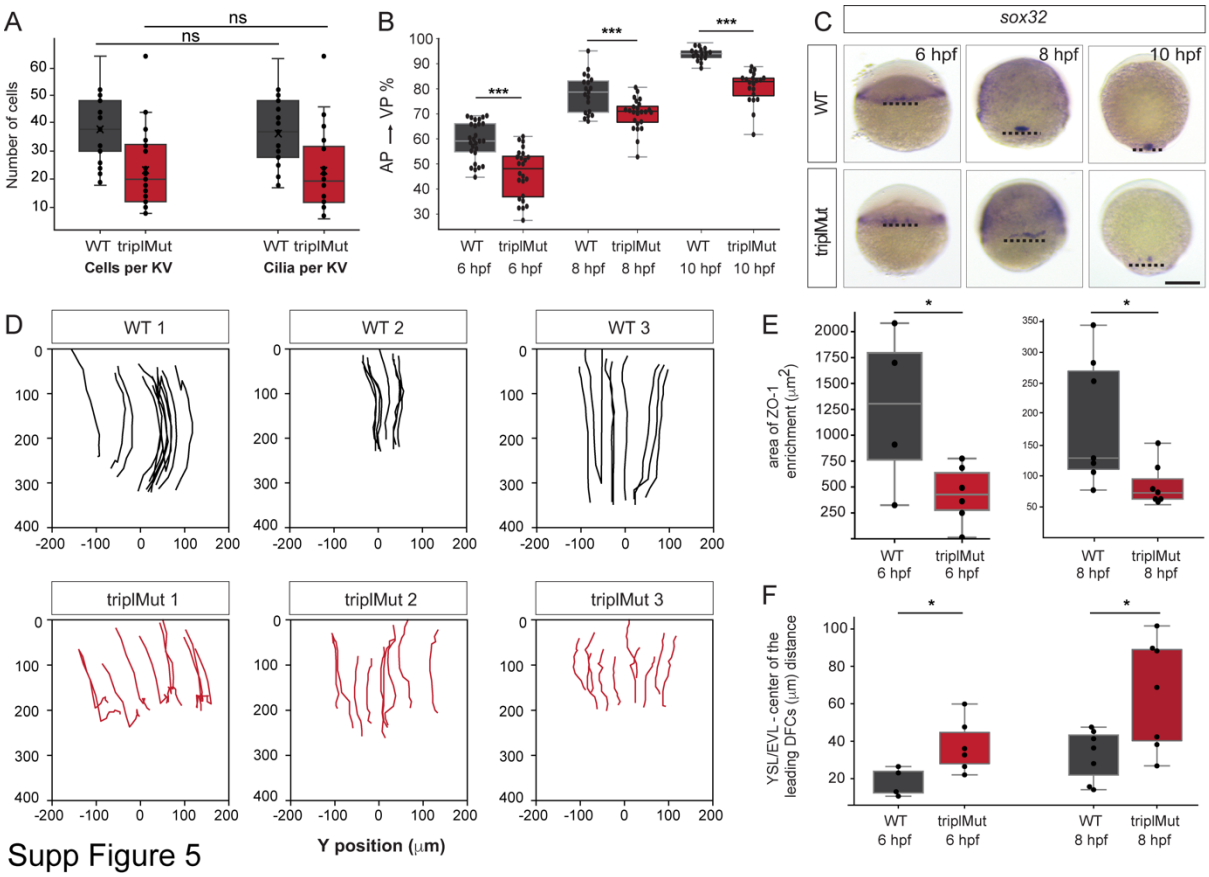

Supp Figure 5

Fig. S5. *Metrns* loss-of-function leads to DFC disorganization and migration defects. (**A**) The KV cilia number and cells per KV quantification in WT and triplMut embryos at 14 hpf show no significant difference between cilia number and KV cells (N WT: 23, N triplMut: 26, Student T-tests, n.s.: 0.67 for WT KV cells, 0.96 for triplMut KV cells). (**B**) DFC migration quantification calculated as the percentage of the total embryo length at 6, 8 and 10 hpf in wild type (WT) *vs*. triplMut embryos. Per condition and group 16 to 27 embryos were analyzed (Fisher exact test, ***p*-value: 2.5e-06 for 6 hpf, ***p*-value: 0.00038 for 8 hpf and ***p*-value: 1.1e-08 for 10 hpf). (**C**) *Sox32* antisense riboprobe *in situ* hybridization highlighting DFC migration between 6 hpf and 10 hpf in WT and triplMut embryos (point line marks the margin of epiboly). All depicted images are dorsal views. (**D**) Single traces of *in vivo* tacked DFCs in WT control (upper panel) and triplMut (lower panel) showing the vegetal movement and convergence. (**E**) Quantification at 6hpf (left plot) and 8 hpf (right plot) of of DFC adjacent ZO-1 enrichments areas reveal a decreased in triplMut embryos in contrast to respective WT controls (T-test; 6hpf **p*-value: 0.043, 8hpf **p*-value: 0.028). (**F**) The distance of the leading DFCs to the EVL is increased in triplMut compared to WT controls visualized at 6 hpf and 8 hpf (nested T-test, **p*-value: 0.039 N = 4 WT, 30 DFCs measured,

triplMut N = 6, 46 DFCs measured; for 6 hpf and *p-value: 0.021 N = 7 WT embryos, 47 DFCs measured, N = 7 triplMut, 54 DFCs measured for 8 hpf). Scale bars: in (**C**) 0.25 mm.

1017

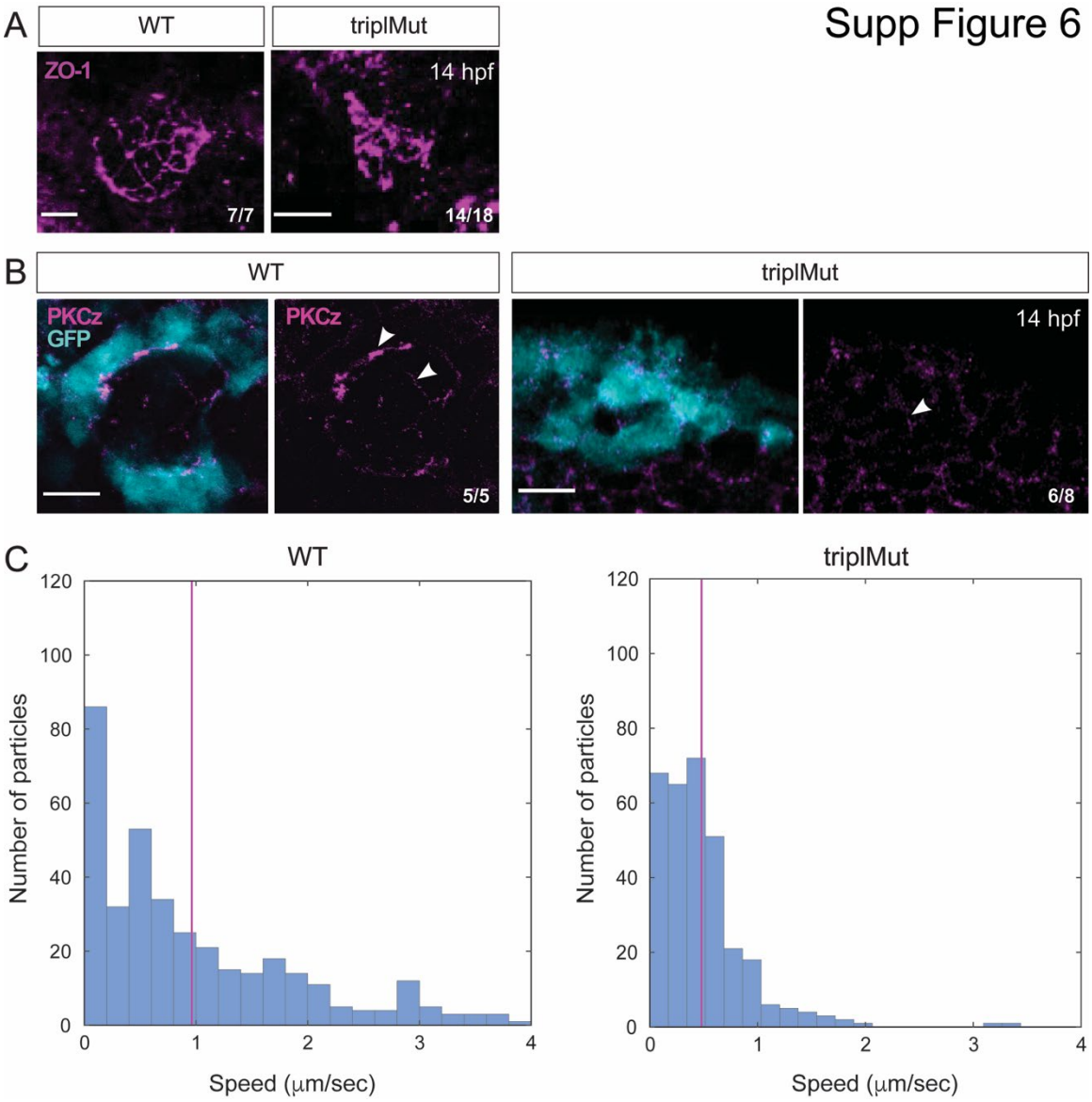

Fig. S6. *Metrns* loss-of-function impairs the Kupffer's vesicle formation and function. (**A**) Dorsal views of 14 hpf wild type (WT) and triplMut embryos immunostained with ZO-1. Wild type embryos display a large KV lumen with uniform ZO-1 labeled tight junction lattice. TriplMut embryos show disturbed KV lumen and dysmorphic ZO-1 lattice. (**B**) WT KV cells of 14 hpf *Tg*(*sox17*:GFP) show proper polarization as visualized with anti-αPKCζ immunostaining (white arrowhead). 14 hpf TriplMut embryos in contrast exhibit a reduced polarization (white arrowhead). (**C**) Tracked microbeads velocity analysis in 12-14 hpf WT and triplMut embryos. The purple line marks the mean and the standard deviation (std) for each condition (WT mean= 0.96212; std=0.048143; TriplMut mean=0.47996; std=0.023682). Scale bars: in (**A-B**) 20 μm.

1018

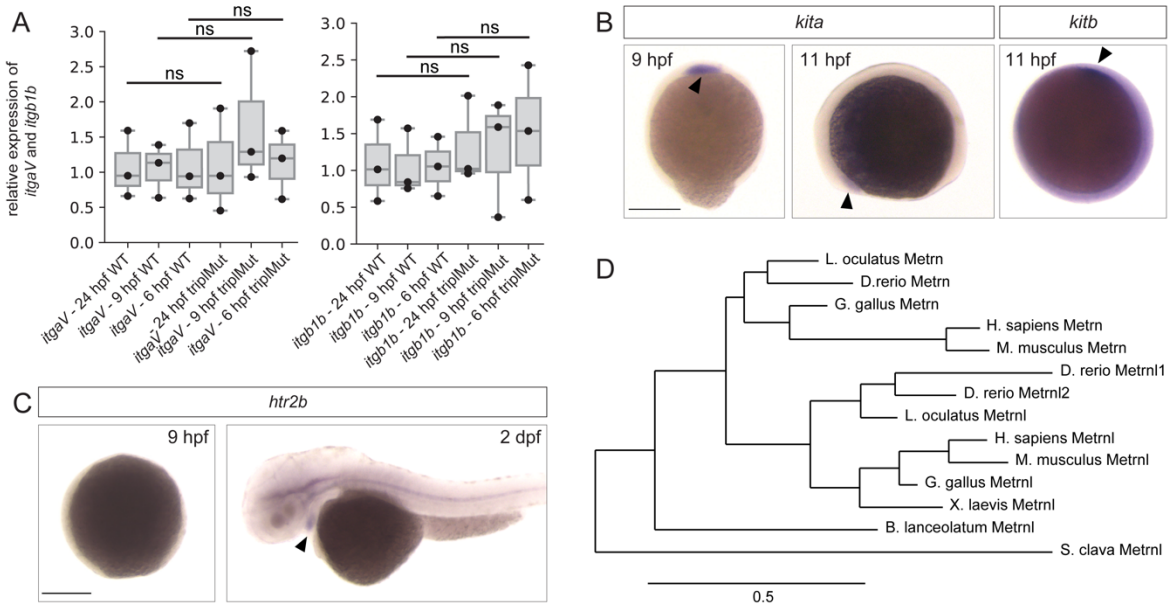

Fig. S7. *Kita, kitb* and *htr2b* expression patterns during early zebrafish development. (**A**) qRT-PCR analysis for *itgaV* and *itgb1b* expression in 6 hpf, 9 hpf and 24 hpf wild type (WT) and triplMut embryos (Fisher exact tests, n.s. = non-significant, *p*-values: 0.95 for 24 hpf *itgaV* WT *vs*. *itgaV* triplMut, 0.37 for 9 hpf hpf *itgaV* WT *vs*. *itgaV* triplMut, 0.92 for 6 hpf *itgaV* WT *vs*. *itgaV* triplMut, 0.64 for 24 hpf *itgb1b* WT *vs*. *itgb1b* triplMut, 0.7 for 9 hpf *itgb1b* WT *vs*. *itgb1b* triplMut, 0.46 for 6 hpf *itgb1b* WT *vs*. *itgb1b* triplMut) (**B**) At 9 hpf *kita* is expressed in the prechordal plate (black arrowhead, dorsal view) and from 11 hpf in the lateral borders of the anterior neural plate (black arrowhead, lateral view). *Kitb* expression could be detected from 11 hpf in the anterior ventral mesoderm (black arrowhead, lateral view). (**C**) At 9 hpf, *htr2b* is not yet expressed. From 2 days post-fertilization (dpf), *htr2b* transcripts could be detected in the developing heart (black arrowhead, lateral views). (**D**) Phylogenetic tree of Metrn proteins. (Scale bar indicates number of amino acids substitutions per site). Scale bars: in (**B – C**) 250 µm.

1019

1020 ## SUPPLEMENTARY VIDEOS
1021
1022 **Video S1:** *In vivo* imaging of GFP-positive DFCs (single cells labelled with *H2B-mRFP* mRNA, full stack)
1023 in a WT (WT 2 from Fig. S5D) embryo from 50% epiboly for 3 hours showing directed DFC movement
1024 and clustering.
1025
1026 **Video S2:** *In vivo* imaging of GFP-positive DFCs (single cells labelled with *H2B-mRFP* mRNA, full stack)
1027 in a triplMut embryo (triplMut 2 from Fig. S5D) from 50% epiboly for 3 hours showing directed DFC
1028 movement, but clustering defects.
1029
1030 **Video S3:** Microbeads tracking the Kupffer's vesicle of 12-14 hpf wild type embryos showing a distinctive
1031 anti-clockwise rotation.
1032
1033 **Video S4:** Microbeads tracking the Kupffer's vesicle of 12-14 hpf triplMut embryos showing the loss of
1034 the distinctive anti-clockwise rotation.
1035
1036
1037 ## SUPPLEMENTARY TABLES
1038

	D-loop	mild/no-loop	S-loop
WT (N = 121)	88.43%	11.57%	0%
***metrn*$^{-/-}$** (N = 131)	61.19%	29.10%	8.21%
***metrnla*$^{-/-}$** (N = 104)	28.85%	51.92%	19.23%
***metrnlb*$^{-/-}$** (N = 104	74.21%	21.38%	4.41%
triplMut (N = 134)	38.17%	25.95%	35.88%
triplMut$^{+/-}$ (N = 182)	85.16%	14.29%	0.55%
triplMut + *metrnla* mRNA (N = 160)	37.5%	53.13	9.37%
triplMut + *metrn* mRNA (N = 156)	45.51%	42.31%	12.18%
triplMut + *metrnla* + *metrn* mRNA (N = 162)	52.47%	27.16%	20.37%

1039
1040 **Table 1:** Quantification of heart looping phenotypes at 2 dpf using *myl7* riboprobe *in situ* hybridization
1041 on wild-type (WT), *metrn*s single and triple mutants (triplMut) and *metrn* and/or *metrnla* mRNAs -injected
1042 embryos. 'Mild/no loop' designates hearts with no particular L-R orientation. D-loop, dextral loop;
1043 mild/no-loop and S-loop, sinistral loop.
1044

	WT-like (% of embryos)	DFC clustering defects (% of embryos)
WT (N = 202)	93.07	6.93
metrn$^{-/-}$ (N = 140)	63.57	36.43
metrnla$^{-/-}$ (N = 245)	46.94	53.06

triplMut (N = 182)	34.62	65.38
triplMut$^{+/-}$ (N = 140)	79.51	20.49

1045

1046 **Table 2:** Quantification in percentage of embryos with DFC clustering defects at 9 hpf in WT, *metrn*$^{-/-}$,
1047 *metrnla*$^{-/-}$, triplMut and and triplMut$^{+/-}$ embryos.

1048

	6 hpf	**8 hpf**	**10 hpf**
WT	59.32% (+/- 7.65%, N = 27)	78.18% (+/- 7.94%, N = 19)	93.67% (+/- 2.68%, N = 16)
triplMut	46.26% (+/- 9.83%, N = 24)	69.94% (+/- 6.22%, N = 24)	80.67% (+/- 6.56%, N = 20)

1049

1050 **Table 3:** Quantification of the DFC migration calculated as the percentage of the total embryo length at
1051 6, 8 and 10 hpf in wild type (WT) *vs*. triplMut embryos.

1052

Experiment	**Number of embryos**
WT non injected	346
WT + ctrl MO	192
WT + 0.41 ng *itgαV* MO	208
WT + 0.5 ng *itgβ1b* MO	623
WT + 1.25 ng *itgαV* MO	412
WT + 0.7 ng *itgβ1b* MO	336
triplMut$^{+/-}$ non injected	219
triplMut$^{+/-}$ + ctrl MO	176
triplMut$^{+/-}$ + 0.41ng *itgαV* MO	182
triplMut$^{+/-}$ + 0.5 ng *itgβ1b* MO	559

1053 **Table 4:** Number of embryos with DFC clustering defects at 9 hpf upon *itgβ1b*, *itgαV* or control (ctrl)
1054 morpholino (MO) injection in wild type (WT) or triplMut$^{+/-}$ embryos.

1055

1056